

VANADIUM-DOPED MAGNESIUM OXIDE NANOPARTICLES AS ELECTRODES IN SUPERCAPACITOR DEVICES

by

ABDALLA HROUB

Submitted to the Graduate School of Engineering and Natural Sciences in partial
fulfillment of the requirements for the degree of Master of Science

Sabancı University

June 2023

Vanadium-Doped Magnesium Oxide Nanoparticles as Electrodes in Supercapacitor Devices

APPROVED BY:

Assoc. Prof. Dr. Emre Erdem
(Thesis Advisor)

Asst. Prof. Dr. Feray Bakan-Mısırlıođlu

Prof. Dr. Mehmet Sankır

DATE OF APPROVAL: 23/06/2023

© Abdalla Hroub 2023
All Rights Reserved

ABSTRACT

Vanadium-Doped Magnesium Oxide Nanoparticles as Electrodes in Supercapacitor Devices

Abdalla Hroub

Advisor: Assoc. Prof. Dr. Emre Erdem

Keywords: Magnesium Oxide, Vanadium, EPR Spectroscopy, Supercapacitors, Electrochemical Analysis.

Magnesium Oxide (MgO) occupies a special stature as a material for energy-storage purposes, owing to its abundance, sustainability, and phenomenal electrochemical features. Vanadium (V) is another unique material, where vanadyl ions (V^{4+}) can be utilized as probing agents to reveal information in characterization spectroscopies that require paramagnetic centers, and to introduce extrinsic defects into host materials to enhance the electrochemical properties. Here in, we report V-doped MgO nanoparticles as electrode materials in all-in-one solid-state supercapacitor devices. The prepared samples' structural, morphological, electronic, and optical properties were thoroughly analyzed utilizing XRD, Raman spectroscopy, STEM, EPR, and PL. EPR spectroscopy was employed to analyze the paramagnetic centers induced in the host material and showed that all V-doped samples displayed a V^{4+} characteristic EPR signal. The electrochemical analysis of the assembled symmetric supercapacitors was done using cyclic voltammetry (CV), electrochemical impedance spectroscopy (EIS), and galvanostatic cycling with the potential limitation technique (GCPL). The results reveal that the novel V-doped MgO material displayed excellent capacitance performance between 0 and 1 V, delivering a specific capacitance of 50 F/g at a 10 mV/s scan rate. It also exhibits a maximum energy density of 4.17 Wh/kg, comparable to values obtained from other symmetric supercapacitor configurations. When a booster material like carbon black was added, the specific capacitance value increased dramatically to 1200 F/g at 20 mV/s, values that were never reported before in the literature for MgO-based materials.

ÖZET

Magnezyum Oksit (MgO), bolluğu, sürdürülebilirliği ve olağanüstü elektrokimyasal özellikleri nedeniyle enerji depolama amaçlı bir malzeme olarak özel bir konuma sahiptir. Vanadyum (V), vanadil iyonlarının (V^{4+}) paramanyetik merkezler gerektiren karakterizasyon spektroskopilerindeki bilgileri ortaya çıkarmak, elektrokimyasal özellikleri geliştirmek ve ana malzemelere dışsal kusurlar eklemek için araştırma ajanları olarak kullanılabilir benzersiz bir malzemedir. Burada, hepsi bir arada katı hal süper kapasitör cihazlarında elektrot malzemeleri olarak V katkılı MgO nanoparçacıkları rapor edilmektedir. Hazırlanan numunelerin yapısal, morfolojik, elektronik ve optik özellikleri XRD, Raman spektroskopisi, STEM, EPR ve PL kullanılarak kapsamlı bir şekilde analiz edilmiştir. Konak malzemede indüklenen paramanyetik merkezleri analiz etmek için EPR spektroskopisi kullanılmıştır ve tüm V katkılı numuneler bir V^{4+} karakteristik EPR sinyali göstermiştir. Birleştirilmiş simetrik süper kapasitörlerin elektrokimyasal analizi, döngüsel voltametri (CV), elektrokimyasal empedans spektroskopisi (EIS) ve potansiyel sınırlama tekniği (GCPL) ile galvanostatik döngü kullanılarak yapılmıştır. Sonuçlar, yeni V katkılı MgO malzemesinin 0 ile 1 V arasında mükemmel kapasitans performansı sergilediğini ve 10 mV/s tarama hızında 50 F/g'lik bir özgül kapasitans sağladığını ortaya koymaktadır. Aynı zamanda, diğer simetrik süper kapasitör konfigürasyonlarından elde edilen değerlerle karşılaştırılabilir şekilde maksimum 4.17 Wh/kg enerji yoğunluğu sergilemektedir. Karbon siyahı gibi bir yükseltici malzeme eklendiğinde, özgül kapasitans değeri 20 mV/s'de 1200 F/g'ye, MgO bazlı malzemeler eklendiğinde ise literatürde daha önce hiç bildirilmemiş değerlere önemli ölçüde yükseldiği görülmektedir.

Acknowledgments

No words can truly and sufficiently describe how extremely appreciative and genuinely happy I am for having had the privilege and honor to pursue my postgraduate studies at Sabanci University; an institute that has become a second home for me, in which I was pushed to my very limits to become a better version of myself.

Firstly, I cannot emphasize enough how grateful I am to Assoc. Prof Dr. Emre Erdem for being the first person to embrace me in this incredible academic community, and for making me a member of a beautiful team under his guidance. Prof. Erdem's mentorship, experience, support, and kindness have shown me exactly what I aspire to become as an academician and always proved to be a constant reminder of why I am doing what I am doing in the first place. Thank you, Sir, for being the light that shone upon our darkest of times, always leading with example, and for paving the road to our current and future successes.

Secondly, I would like to point out that none of this would have been possible without all the warmth, team spirit, and guidance my fellow colleagues have shown me during the duration of this two-year-long journey. I have to mention Mohamad Hasan Aleinawi, a colleague who has been by my side since day one, and to whom I owe a lot for what I have learned today. I would also like to thank my colleagues Sumaiyah, Ameen, and Deniz for their constant support, and for making the laboratory feel like a home. Of course, I also cannot stress enough how thankful I am to the esteemed jury members: Assoc. Prof. Dr. Feray Bakan-Misirlioglu and Prof. Dr. Mehmet Sankır for their precious time reviewing and evaluating this work. Furthermore, I dedicate a special thanks to Dr. Arpad Rostas and the entire Romanian collaboration, with whom I have had the honor of publishing my first article, for their incredible cooperation and professionalism.

Last but not least, I want to thank my beautiful family for shielding me from all the storms we experienced the past year, and for showing me the true definition of unconditional love and support. I am also extremely lucky to have friends who believe in me through all the turbulence, and who despite the distance separating us always find ways to show me their love and support.

Table of Content

ABSTRACT	I
ÖZET	II
Acknowledgments	III
Table of Content	IV
List of Figures	VI
List of Tables	VIII
1. Introduction	1
2. State of the Art	7
2.1. Electrochemical Performance of Supercapacitors	7
2.2. Electronic Properties & Defects of MgO	10
2.3. Spectroscopic Features of Vanadyl Compounds.....	12
3. Synthesis of MgO	14
3.1. Chemical Precipitation of MgO:V _x	15
4. Characterization Methods	17
4.1. X-Ray Diffraction (XRD)	17
4.2. Raman Spectroscopy.....	18
4.3. Scanning Transmission Electron Microscopy (STEM).....	19
4.4. Electron Paramagnetic Resonance (EPR) Spectroscopy.....	20
4.5. Photoluminescence (PL) Spectroscopy	21
4.6. Electrochemical (EC) Measurements	22
5. Results & Discussion	24
5.1. X-Ray Diffraction Analysis	24
5.2. Raman Analysis.....	30

5.3.	Scanning Transmission Electron Microscopy Analysis.....	33
5.4.	Electron Paramagnetic Resonance Analysis	37
5.5	Photoluminescence Analysis	42
5.6.	Electrochemical Analysis.....	47
5.6.1.	Cyclic Voltammetry (CV)	47
5.6.2.	Electrochemical Impedance Spectroscopy (EIS)	52
5.6.3.	Galvanostatic Charge-Discharge with Potential Limitation (GCPL)	55
6.	Conclusions.....	59
7.	References	61

List of Figures

Figure 1: A Ragone Plot displaying the energy and power densities of different energy storage devices. Adapted from [19].....	2
Figure 2: Electronic configuration of Mg^{2+} and O^{2-} ions, as well as the crystal structure of MgO. Adapted from [40].....	3
Figure 3: Schematic illustration of possible application fields for vanadium oxides. Adapted from [41].....	5
Figure 4: A schematic illustration of the different classes of SCs: (a) EDLCs, (b) Pseudocapacitors, and (c) ASSCs. Adapted from [50].....	8
Figure 5: Common TMOs and mixed MOs as precursors for electrode materials along with their surface areas. Adapted from [50].....	10
Figure 6: A schematic diagram of the chosen chemical precipitation synthesis method.	15
Figure 7: Bruker EMX Nano device utilized in EPR spectroscopy at Sabancı University (Location: FENS Lab 2110).....	21
Figure 8: Spectrofluorometer FS5 device utilized in PL spectroscopy at Sabancı University (Location: FENS Lab 2110).....	22
Figure 9: A schematic diagram of the tested symmetric supercapacitors constructed from the MgO:V _x samples.	23
Figure 10: X-ray diffractogram of undoped MgO (black), MgO:V0.2 (red), MgO:V0.5 (green), and MgO:V0.7 (blue).....	24
Figure 11: W-H plots for undoped MgO with a linear fit.....	26
Figure 12: W-H plots of MgO:V0.7 with a linear fit.....	26
Figure 13: Average crystalline sizes (D) of the MgO:V _x samples calculated from The Scherrer Equation (Black) and W-H Plots (Red).	27
Figure 14: Rietveld refinement with discrepancy from experimental data and Bragg positions displayed for (a) MgO, and (b) MgO:V0.7.....	29
Figure 15: Raman spectra of undoped and V-doped MgO powder.....	31
Figure 16: EDS and mapping images of the MgO:V0.7 sample showing the main elements O (purple) and Mg (red), as well as the dopant element V (yellow).	32

Figure 17: STEM Images of (a) Undoped MgO, (b) MgO:V0.2, (c) MgO:V0.5, and (d) MgO:V0.7.	34
Figure 18: Histograms fitted with a Gaussian curve (left) and log-normal distribution (right) to calculate the average particle sizes of undoped MgO and MgO:V0.7.	35
Figure 19: Diagram of a MgO supercell. Red: O ions, Black: Mg ions, Blue: Mg vacancy, Empty Dotted Spheres: O vacancy. Adapted from [61].	38
Figure 20: X-band EPR spectra of the MgO:V _x samples.	38
Figure 21: Q-band EPR spectra of the MgO:V _x samples. The pink dashed lines portray MgO intrinsic defects, whereas the purple dashed lines show the well-resolved hyperfine lines due to the V ⁴⁺ ions.	39
Figure 22: X-band Aniso-Spin fits of the MgO:V _x samples (50 scans at a power of 3.162 mW).	40
Figure 23: The electron spin density of the MgO:V _x samples.	41
Figure 24: PL spectra of the MgO:V _x samples.	42
Figure 25: A free-electron model demonstrating possible electron-hole recombination. The blue-filled circles represent occupied electronic states, whereas the white ones represent vacant electronic states or holes. White circles in the valence band demonstrate cationic holes.	43
Figure 26: Tauc plots of undoped MgO (left) and MgO:V0.7 (right).	45
Figure 27: A visual demonstration of the bandgap energies of undoped MgO (left-side) and MgO:V0.7 (right-side).	46
Figure 28: Cyclic voltammetry of the MgO:V _x samples carried out between 0 and 1 V at a scan rate of 50 mV/s.	47
Figure 29: <i>C_p</i> values obtained for MgO:V _x samples from CV curves at a scan rate of 50 mV/s.	49
Figure 30: CV of the MgO:V0.7 sample carried out between 0 and 1 V at different scan rates.	50
Figure 31: <i>C_p</i> values obtained for the MgO:V0.7 sample at different scan rates.	50
Figure 32: <i>C_p</i> values plotted as a function of the scan rate for the MgO:V0.7 sample in symmetric (below) and CB-asymmetric (above) supercapacitor devices.	52
Figure 33: Nyquist Plot of the MgO:V _x supercapacitor devices. The inset highlights the high-frequency zone.	53
Figure 34: Z-Fits & equivalent circuits of Nyquist Plots in the high-frequency zone of undoped MgO (left-side) and MgO:V0.7 (right-side)	54

Figure 35: A Ragone Plot showing the energy and power densities for the MgO:V_x samples. .. 56

Figure 36: GCPL electrochemical reversibility assessment for undoped MgO (left-side) and MgO:V_{0.7} (right-side). 57

Figure 37: GCPL cyclic stability assessment for (a) undoped MgO, and (b) MgO:V_{0.7} through a measure of capacity retention and coulombic efficiency..... 58

List of Tables

Table 1: Detailed information about the chemicals used in the precipitation synthesis of MgO:V_x. 16

Table 2: Definition and description of the notations used to describe the MgO:V_x samples. 16

Table 3: Lattice parameter, unit cell volume and occupancy of individual atoms in the structure. 28

Table 4: A summary of the values of the electronic parameters comprising the equivalent circuits..... 54

1. Introduction

In the past decades, the reliance on fossil fuels as a primary energy source has drastically decreased as the world has shifted to cleaner and more diverse power solutions (e.g., solar, wind, geothermal, nuclear, water electrolysis, and biomass energy) to satisfy the blooming energy requirements of the 21st century [1-4]. Accordingly, energy storage systems have become the fundamental basis for storing the surplus of energy harvested from renewable sources to be utilized upon demand later due to their intermittent nature. Among different energy storage devices, supercapacitors have acquired significant attention in recent years due to their ability to bridge the gap between batteries and capacitors, combining a relatively high-power density with a long cycling life as illustrated in Figure 1 [5]. Nonetheless, one of the main drawbacks of supercapacitors remains that their energy densities are relatively low compared to batteries [6]. Consequently, many research efforts addressed this issue, focusing on one of the key components of these energy storage devices: the electrode materials [7].

Ideal material candidates for electrodes exhibit large surface areas, high electrical conductivities, controllable porosities, and good chemical stability with the consideration of cost-effectiveness [8]. Metal oxides are investigated as potential electrode materials and have been proven to exhibit all the properties above, increasing the specific capacitance drastically [9]. Transition metal (TM) oxides such as ZnO [10, 11], MnO₂ [12], Co₃O₄ [13] as well as complex iron oxides like FeCo–Fe₂CoO₄/Co₃O₄ [14] and BaFe_{12-x}Al_xO₁₉ (with x = 0.1-1.2) [15] have all demonstrated high power densities and capacities when used as electrodes, with major structural defects [16]. Such defects modify the electrical/chemical characteristics of the materials, influencing the redox reactions occurring in supercapacitors during charge/discharge cycles, where significant parameters such as the roughness, porosity, and surface area of the electrodes are enhanced. Defects like metal and oxygen vacancies create different active sites to facilitate ion adsorption/desorption, resulting in higher capacitance/conductivity and ultimately increasing the energy and power densities of the devices [17]. Another way to improve electrical properties is the combination of different compounds which have excellent electronic properties, leading to new composite materials which have earned great technological interest in recent years. Adding

a second phase can significantly improve the electronic properties of the resulting composite [18].

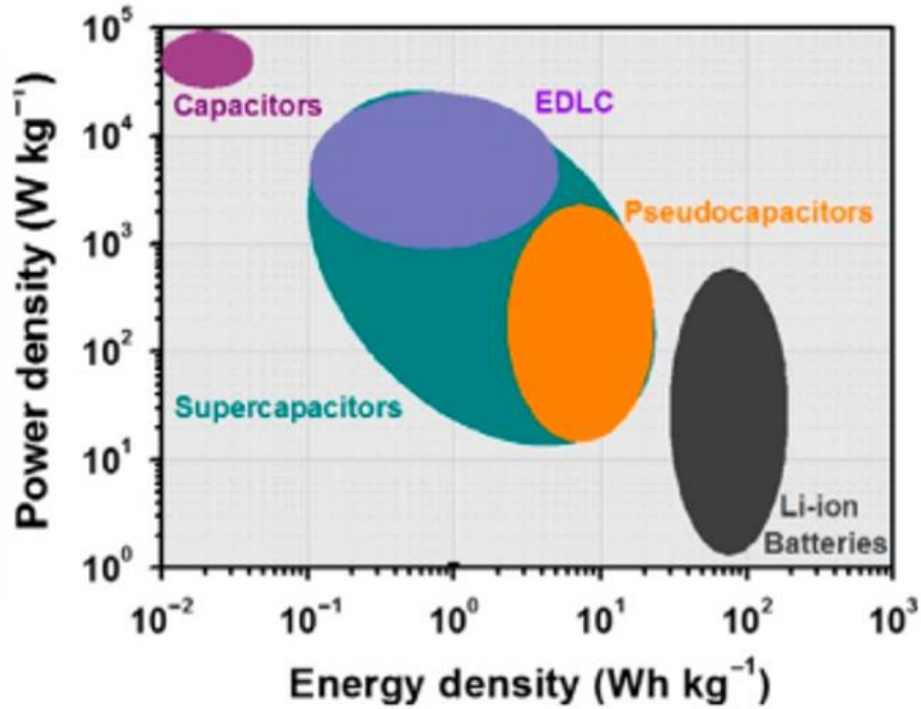


Figure 1: A Ragone Plot displaying the energy and power densities of different energy storage devices. Adapted from [19].

Even though defects might be perceived as imperfections that negatively affect material properties, sometimes they result in improving the material's electrical, magnetic, optical, catalytic, and energy-conversion features [20-24], which are crucial, especially in industrial and technological applications associated with sensors, adsorbents, catalysts, supercapacitors, and luminescence devices [25-29]. Consequently, inducing material defects to attain desirable properties has become a vital research area, which includes magnetic features in graphene [30], plasmonic properties in Si nanocrystals, ferroelectric characteristics in CuO [31], electrochemical features in MgO [32], and photoluminescence properties in ZnO [33, 34], CuO, and MgO [35-39].

Magnesium Oxide (MgO), also referred to as Periclase, is a white, odorless, and non-flammable solid used in a wide range of applications, mainly as a refractory material in high-temperature applications. It is an inorganic compound with a molar mass of approximately 40.31 g/mol and a density of 3.58 g/cm³. Mg²⁺ and O²⁻ ions, with 1s²2s²2p⁶ electronic configurations, ionically bond to form a rock-salt type MgO crystal structure with a lattice parameter of 4.21 Å, as portrayed in Figure 2 [40]. Recently, MgO has been attracting attention as a promising material for research. However, much of the information regarding the effect of MgO's electronic structure on the material's properties has still not been fully explored in the literature.

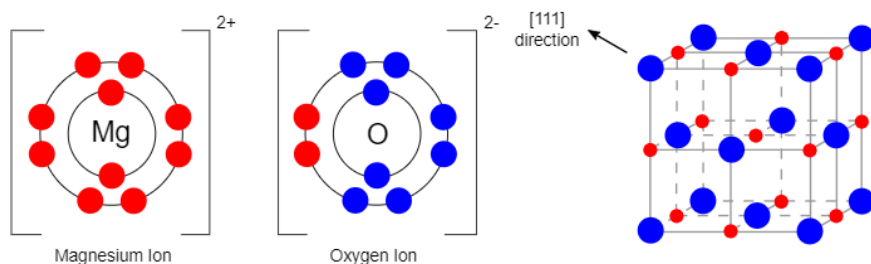


Figure 2: Electronic configuration of Mg²⁺ and O²⁻ ions, as well as the crystal structure of MgO. Adapted from [40].

MgO nanoparticles, nano-powder, and nanodots, typically 5 nm to 100 nm in size, are spinel and exhibit high surface areas, with specific surface areas ranging between 25 m²/g and 50 m²/g. MgO possesses several electrochemical features that make it a good candidate for electrode material. Firstly, MgO is a chemically stable compound with a high melting point that has good resistance against acid/base corrosion in a variety of electrolytes. Secondly, in its natural form, MgO is a good insulator, due to the lack of mobile electrons, but can become conductive in the presence of intrinsic and/or extrinsic defects (doping with impurities). Thirdly, MgO has a high dielectric constant value, signifying a promising ability to store electrical energy in capacitors. Furthermore, it is a redox-active compound that easily participates in Faradic reactions when immersed in a suitable electrolyte [40].

Although much of the information regarding the effect of MgO's electronic structure on the material's properties has still not been fully explored in literature, MgO has the potential to be an effective electrode material in supercapacitors due to several reasons. It has a high specific

surface area (25 m²/g - 50 m²/g) that provides a large active surface for faradic reactions to occur, thus resulting in high capacitances and ultimately energy densities. It also has a high electrical conductivity which facilitates an efficient electron transfer mechanism between the electrodes. Furthermore, the fact that Mg is one of the most abundant elements on the planet implies the low cost and availability of MgO, thus making it a good choice for large-scale energy applications. Nonetheless, utilizing MgO electrodes in supercapacitors is associated with some challenges. During charging/discharging cycles, MgO undergoes changes in volume, which in turn results in the degradation of the structure, thus a decreased cycling stability. Also, in some electrolytes MgO can display poor solubility, thus restricting the rate of ion transfer and the electrochemical performance of the device [40].

Vanadium (V) has been first discovered by Mexican scientist Andrés Manuel del Río Fernández in 1801, only to be later rediscovered in 1830 by Swedish scientist Nils Gabriel Edstrom. It is classified as the 5th most abundant transition metal, and the 19th most abundant element, with typical oxidation states alternating from +2 to +5. Vanadium is mainly utilized in industries to enhance alloy steels and cast irons with better ductility and shock resistance. The pure form of vanadium, like a typical transition metal, displays a high melting point with good resistivity against corrosion at reduced temperatures. Nonetheless, it is quite challenging to find pure vanadium in its metallic form in nature, as it readily reacts with oxygen, nitrogen, and carbon at high temperatures [41].

Vanadium has an electronic configuration of [Ar]4s²3d³, where vanadium oxides possess crystalline structures with alternating oxygen coordination, thus resulting in the production of octahedral, pentagonal-bipyramidal, square-pyramidal, and tetrahedral structures. The physiochemical properties of vanadium oxides (color, morphology, density, etc..) are strongly influenced by the oxidation state of the vanadium cations. The various oxidation states and possible crystalline structure morphologies of vanadium oxides lead to superior intercalation features to ions, outstanding catalytic properties, enhanced electron-electron correlations, and excellent phase transitions and electrical conductivities as demonstrated in Figure 3. Different synthesis methods of vanadium oxide can be manipulated to facilitate a shorter transportation distance of electrons/ions, a more rapid solid-state diffusion in electrochemical energy

conversion systems, more active sites for ion interactions, and more exposed active crystal facets for catalysis [41].

Vanadyl compounds have been recently investigated as potential electrode materials for supercapacitors. The layered structure of vanadium oxide eases the flow of ions during charging/discharging. The high specific capacitance of vanadium oxide signifies its ability to store relatively large amounts of energy and combined with its low cost and abundance makes it ideal for use as an electrode material. However, vanadium oxide displays poor conductivity in a range of different electrolytes, thus limiting its electrochemical performance. Producing vanadium oxide nanoparticles (increasing the surface area to volume ratio), and/or doping with other conductive materials drastically improves the electrical properties of vanadyl compounds [42].

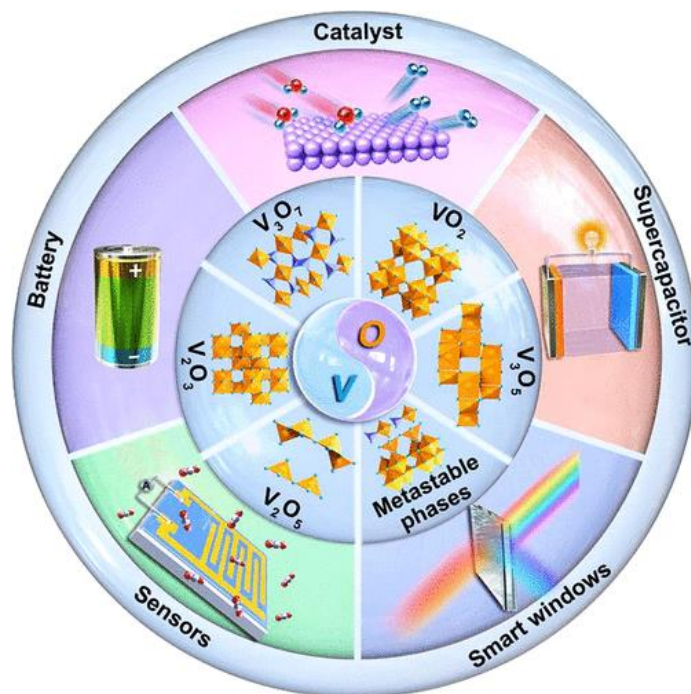


Figure 3: Schematic illustration of possible application fields for vanadium oxides. Adapted from [41].

In this thesis, MgO was doped with different V^{4+} concentrations and utilized as electrodes in symmetric supercapacitor devices. The different V-doped MgO samples are referred to with the annotation $MgO:V_x$, where x stands for the doped V^{4+} mole percentage in MgO. In the first

chapter to follow, a thorough literature review regarding the types and electrode materials for supercapacitors, and the electrochemical properties of MgO and vanadyl compounds is presented. Furthermore, possible synthesis routes for MgO are briefly compared in Chapter 3, and the chosen method is illustrated in further detail. Moreover, different morpho-structural characterization techniques like X-Ray Diffraction (XRD), Raman spectroscopy, Scanning Transmission Electron Microscopy (STEM), Photoluminescence (PL), and Electron Paramagnetic Resonance (EPR) spectroscopy were employed to characterize the materials, and equipment specifications were presented in Chapter 4. Subsequently in Chapter 5, an analysis of the data obtained from the aforementioned characterization methods led to valuable information about the intrinsic defects in the MgO samples, and the extrinsic defects introduced with V-doping. Firstly, XRD data was processed, where the Scherrer Equation and Williamson-Hall plots were utilized to calculate the average crystalline size of the samples. A Rietveld refinement was conducted to further investigate the effect of doping on the lattice parameters of the crystal solid. Secondly, to complement the XRD analysis, Raman analysis was performed to probe the phononic mode changes occurring in the MgO crystals due to V-doping. Thirdly, TEM analysis led to a better understanding of the crystalline morphology and average particle size, while PL analysis led to the calculation of the bandgap energies of the different samples. Fourthly, EPR analysis (X-band and Q-band) was conducted to investigate the intrinsic defects in the undoped MgO sample, and extrinsic defects associated with doping. Finally, the V-doped and undoped MgO-based materials were tested as electrode materials in symmetric supercapacitors. Their electrochemical properties were evaluated through Cyclic Voltammetry (CV), Electrochemical Impedance (EIS) Spectroscopy, and Galvanostatic Cycling with Potential Limitation (GCPL). The MgO:V_x sample displaying the best electrical properties was then used with carbon black in the construction of an asymmetric supercapacitor device.

2. State of the Art

2.1. Electrochemical Performance of Supercapacitors

In recent years, the necessity to preserve natural resources and to regulate worldwide energy consumption has become evident leading to vital demand for the design and development of clean energy sources, as well as devices to store the intermittent energy produced from renewable sources. Among a variety of different energy storage devices, such as batteries, fuel cells, and capacitors, supercapacitors have attracted a lot of research attention due to their superior electrochemical features, including high power densities, stable cycling life, and fast charge/discharge rates [43]. Supercapacitors, otherwise referred to as ultracapacitors or electrochemical capacitors, comprise an electrolyte, a current collector, large specific surface area electrodes, and dielectric separators that aid in increasing the capacitance to values higher than those exhibited by conventional batteries and capacitors [44]. The charge/discharge processes occurring at the electrode–electrolyte interface dictate the energy storage mechanism in supercapacitors, similar to the working principle of capacitors, but with the exception that the charge/discharge rate is much more rapid. While conventional values of stored charge in capacitors range from micro to millifarads, supercapacitors can store charge from 100 F up to 1000 F, maintaining low equivalent series resistance [45]. The energy density is a measure of the usage duration of the energy storage device, whereas the power density is an indication of how fast the device can deliver that stored energy. Depending on the design of the supercapacitor devices, as well as the materials involved, the power and energy densities can exceed those of batteries. Furthermore, supercapacitors are superior to batteries and capacitors (lacking a dielectric material) in terms of safety, reduced heating, device stability, greater portability, and more flexible packaging [46].

Supercapacitors can be classified into three main types: Electric Double Layer Capacitors (EDLCs), Pseudocapacitors, and Asymmetric Supercapacitors (ASSC) as illustrated in Figure 4. EDLCs utilize double-layer electrodes at the electrode–electrolyte interface to electrostatically store the charge through non-faradaic interactions. Pseudocapacitors exploit redox reactions to store the charge through faradaic interactions, where the generated electrons travel across the electrode–electrolyte interface. Asymmetric Supercapacitors merge both faradic and non-faradic

behavior, where the mechanism of charge storage for the cathode is different from that of the anode. Unlike “symmetric” supercapacitors, where both electrodes are identical, “asymmetric” supercapacitors consist of distinct electrodes with different materials. Hybrid Supercapacitors (HSCs) can be considered as a subtype of ASSCs, where the anode is made up of a battery material, and the cathode consists of a supercapacitive material. Consequently, ASSCs, including HSCs, exhibit the highest capacitance, energy density, and power density values with wider voltage windows (depending on the nature of the electrolyte used) as they exploit the advantages of the different electrode materials [47-49].

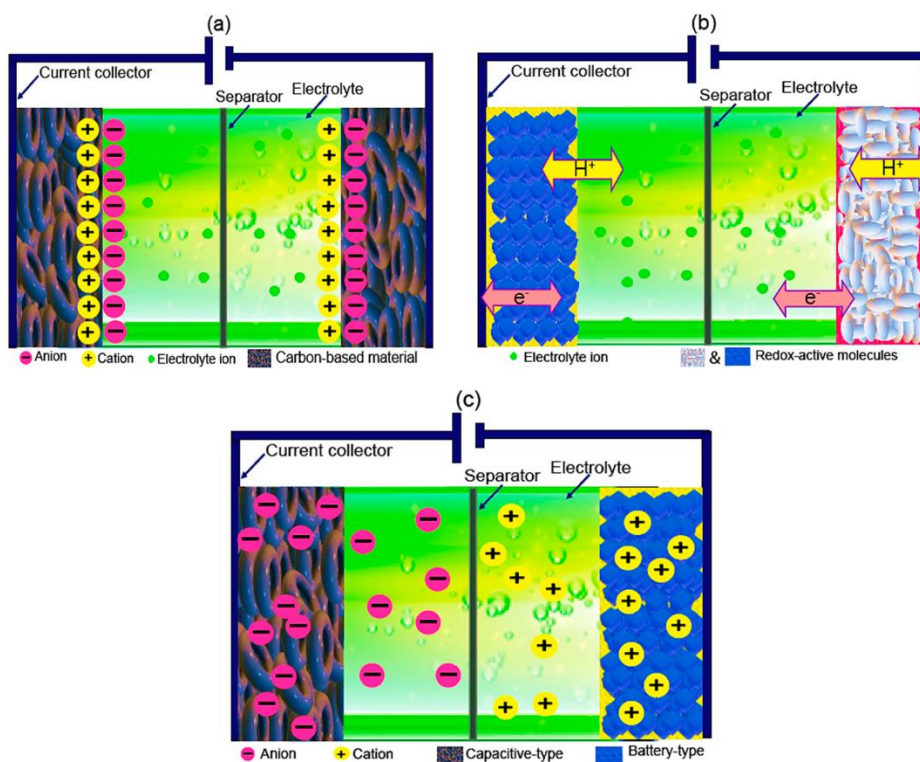


Figure 4: A schematic illustration of the different classes of SCs: (a) EDLCs, (b) Pseudocapacitors, and (c) ASSCs. Adapted from [50].

Capacitance, energy density, power density, cell potential, cycle life, self-discharge, reversibility of the fabricated electrodes, capacity retention, and coulombic efficiency are all significant parameters to characterize the electrochemical performance of supercapacitors and are dependent on the type of electrolyte solution used, and the materials of the fabricated electrodes. Not only do HSCs show superior performance in energy/power densities when compared against Pseudocapacitors and EDLCs, but they also display longer cycling stabilities (up to 100,000

cycles), and lower self-discharge or energy dissipation caused by redistribution of charges, parasitic faradaic reactions, and/or ohmic leakage [51, 52].

Fabricating the electrodes with the selection of suitable materials is crucial to improve the aforementioned electrochemical parameters of SCs. The fabricated electrodes should exhibit high specific surface areas and electrical conductivities, good thermal and chemical stability, resistance against corrosion, no negative externalities to the environment, and should be cost-effective [53]. Aside from the specific surface area of electrodes, the electrolyte pore morphology (pore size distribution and shape) influences the specific capacitance. Therefore, when designing a SC device, large surface area electrodes should be used to improve the electrochemically active sites, and the pore morphology should be tuned in a way that allows maximal facilitation of electrolyte ions [54]. There is usually a trade-off between energy and power density, where reducing pore sizes in electrodes results in higher capacitance and energy density at the expense of higher equivalent series resistance, thus lower power density. However, optimizing the pore size distribution in the electrode material can enhance the retention capability of SCs leading to higher power densities since an effective pore morphology affects the rate of mass and ion transport through the electrolyte [55]. Electrode materials are classified into three main types: carbon-based electrodes, transition metal oxide (TMO) materials, and conducting polymer electrodes. HSCs mostly operate with transition-metal-based electrodes, either in the oxide or hydroxide form, owing to their high activity in redox reactions. TMOs are commonly utilized as pseudocapacitive electrode materials since they display rapid and reversible redox reactions that result in high capacitances and cycling stability [56]. Common TMOs reported in literature to exhibit faradic behavior in charge storage as electrodes are displayed in Figure 5 [10, 57-59].

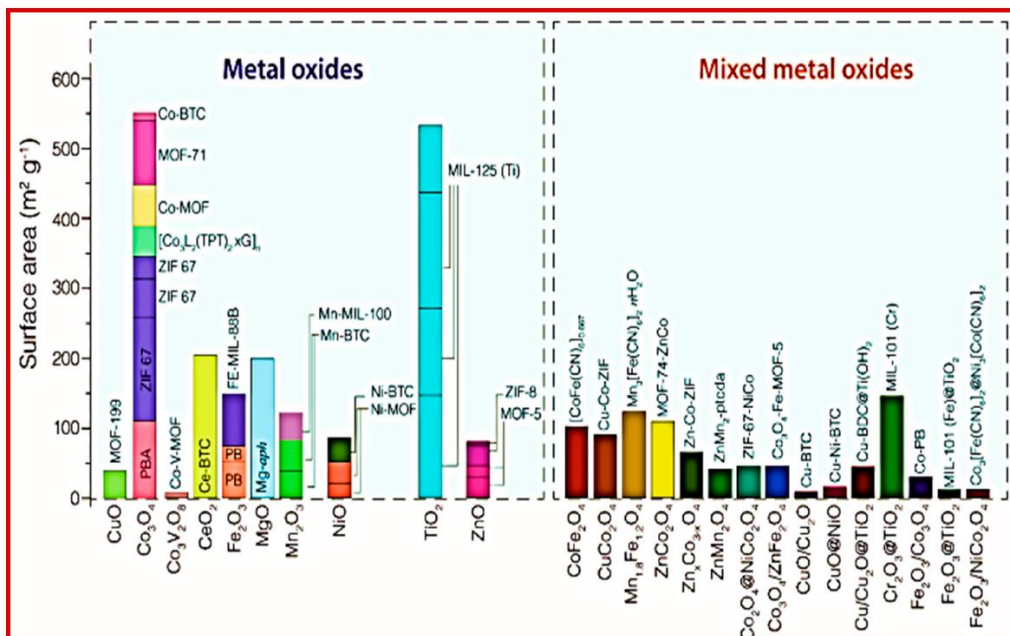


Figure 5: Common TMOs and mixed MOs as precursors for electrode materials along with their surface areas. Adapted from [50].

2.2. Electronic Properties & Defects of MgO

MgO is a wide band gap insulator with a band gap energy of 7.8 eV (bulk form), with unique electrical, magnetic, and photoluminescent properties due to various structural defects such as Mg/O vacancies, interstitial, and Schottky defects [60]. However, intrinsic and extrinsic defects in MgO decrease the material's photon excitation energy drastically below 7.8 eV, as multiple electronic states are produced within the wide band gap [61]. Possible intrinsic defects include: (a) Mg vacancies (V_{Mg}^0 , V_{Mg}^{-1} , V_{Mg}^{-2}), (b) Mg interstitial substitution (Mg_i), (c) O vacancies (F , F^+ , F_2^{1+} , F_2^{2+} , F_2^{3+}), (d) O interstitial substitution (O_i , O_i^{-1} , O_i^{-2}), and (e) Schottky defects. It is worth mentioning that F_s , rooting from the German word Farbe (meaning color), signifies colored centers attributed to oxygen vacancies due to light activity, where the subscript "s" denotes the center's location on the surface. Although a more common notation for O vacancies is V_{O} , the F_s nomenclature will be crucial in explaining color-centered defects in Chapter 5.5. Pathak *et al.* reported that several of the desired magnetic and optical properties in the visible region of MgO are caused by O vacancies (F^+) and their clusters (F_2^{2+}) [62]. Furthermore, they

found that altering the synthesis conditions, performing a thermal treatment, and applying irradiation change the concentration of paramagnetic defect centers in MgO, thus affecting the ferromagnetic behavior of the semiconductor.

An alternative approach to induce defects in the MgO structure is doping with different transition metals (e.g., Mn, Co, and Zn) or rare earth metal ions (e.g., Eu^{2+} / Eu^{3+} , Ce^{4+} , Gd^{3+}) to improve the catalytic, luminescence, and electrical properties [63, 64]. For example, doping MgO with Ce^{4+} improves its catalytic abilities in industrial areas such as automotive exhaust treatment, water treatment, and fuel cells [65]. Several studies have been reported in literature on the doping of MgO with different transition metals. Kantam *et al.* doped MgO nanocrystals with ruthenium nanoparticles, incorporating choline hydroxide to catalyze the hydrogenation of different carbonyl compounds [66]; Layek *et al.* described the synthesis of an excellent catalyst by doping MgO with gold nanoparticles, followed by sodium borohydride reduction, via counterion-stabilization route [67]; and Wang *et al.* reported the synthesis of very stable super magnetic nanoparticles comprising of Mg, Mn, and Fe via the sol-gel route, and with the aid of diethyl glycol as a reducing agent [68].

EPR spectroscopy is essential here to identify the defects in the MgO structure, allowing a clear comparison between intrinsic defects already present in the undoped MgO sample, and extrinsic defects forming as V dopant is introduced into the crystal structure. It should be noted that EPR spectroscopy is sensitive to paramagnetic species only and that by calculating the g-factor at sites where the resonance condition is achieved, it becomes possible to speculate about the type of defects attributing to the corresponding signals. The EPR spectra of pure undoped MgO do not show any characteristic lines due to the lack of unpaired electrons. However, Pathak *et al.* demonstrated that as MgO is annealed at higher temperatures, intrinsic defects are generated in the system (e.g., Mg/O vacancies), leading to sharpened intensities on the lower field side with four unique signals at $g = 1.96$, $g = 1.98$, $g = 2.03$, $g = 2.07$ [62]. This makes sense since MgO is not a paramagnetic material yet heating the compound spurs thermal dissociation in the clusters, increasing the concentration of cationic vacancies. Ramadevudu *et al.* performed studies on a ternary glass system of $\text{MgO-R}_2\text{O-B}_2\text{O}_3$ doped with V^{4+} ions. Applying an EPR analysis with X-band at 303 K, they found that V^{4+} exists as VO^{2+} ions, occupying an octahedral coordination with tetragonal compression in the glass system [69]. Furthermore, Boldu *et al.* characterized

sol-gel Li/MgO catalysts with EPR demonstrating that irradiating the synthesized catalyst is not sufficient for activation; however, when coupled with low-temperature measurements utilizing liquid nitrogen, catalyst activity is optimized [70].

2.3. Spectroscopic Features of Vanadyl Compounds

Recently, VO^{2+} has attracted much attention as an EPR spin probe of systems in applications of biochemistry, materials science, and other fields [71]. The spectroscopic features and chemical properties of V^{4+} make it of particular prominence as a probe ion introduced into EPR silent crystal structures. However, probing with V^{4+} should be performed under a nitrogen atmosphere or with the aid of a reducing agent since at pH values around 7, VO^{2+} is oxidized by air to form V^{5+} , an EPR silent ion [71]. Among the different oxidation states of vanadium, V^{4+} ions are the most stable oxygen-containing ions of the first-row transition metal ions, forming under physiological conditions. The oxo unit in VO^{2+} enables V^{4+} to replace divalent cations, thus forming strong anionic, cationic, and neutral complexes with almost any type of ligand. Furthermore, the vanadyl oxygen in V^{4+} tends to always occupy one coordination position, thus extrinsically defecting metals with VO^{2+} alters the metal-binding sites in the ligand geometry. Such site distortions associated with V^{4+} doping are utilized for probing purposes and have not been reported in literature to induce any prominent issues [71].

The electromagnetic properties of vanadyl compounds make them excellent paramagnetic probes in spectroscopy upon doping in EPR-silent diamagnetic compounds like MgO. When V-containing compounds undergo hydrolysis, changing color from blue to green, vanadyl ion VO^{2+} is generated with a coordination number of 5 and a square pyramidal structure. Vanadyl compounds exhibit a characteristic g factor of 1.968, less than that of a free electron. When a magnetic field is applied, the unpaired electron in the d orbital ($3d^1$) of the vanadyl ion orients itself either parallelly or antiparallelly to the field vector. This generates two energy levels with spin quantum numbers $m_s = \pm 1/2$. Since the ground state nuclear spin quantum number of V^{4+} is $I = 7/2$, hyperfine interactions between I and the electron spin operator, S, occur, resulting in the additional splitting of the electronic states into $2I + 1$ sublevels. The aforementioned interactions result in an EPR spectrum with a set of 8 lines with alternating intensities. Among the different

paramagnetic metal ion complexes, it has been reported that only VO^{2+} consistently displays a sharp and defined EPR spectrum in both room temperature and frozen solutions [72]. This is particularly important for biological applications, extending the range of possible experimentations, and making it easier to characterize any equilibria shifts occurring from reducing the temperature to the freezing point.

Many researchers have investigated the effect of pH, temperature, and ball-milling on the EPR signals produced. Chasteen *et al.* have reported that at a neutral pH, VO^{2+} oligomerizes into $(\text{VOOH})_2^+$, and thus becomes EPR silent [72]. They further found that as the pH is reduced V (IV) stabilizes in coordination complexes and produces EPR signals in the X-band. Furthermore, Pathak *et al.* reported that heating vanadyl compounds reduces the intensities of these lines until they completely vanish after calcination at 600 °C due to the complete oxidation of vanadyl ions into V^{5+} ions, which are insensitive to EPR ($3d^0$ – no unpaired electron) [73]. Moreover, Kolbanev *et al.* portrayed the effect of ball-milling on the generated EPR signals of Molybdenum – Vanadium Oxide [74]. It was experimentally illustrated that as the time duration of mechanical degradation is increased, two main differences are noticed: (a) EPR lines are drastically broadened, and (b) a broad anisotropic single line superposes with the initial multiplet spectrum. The latter observation verifies the formation of high-concentration paramagnetic centers with increased ball-milling [74].

3. Synthesis of MgO

A wide range of different synthesis routes is described in the literature for obtaining MgO nanostructures, among which the most common are

- sol-gel method,
- hydrothermal/solvothermal method,
- solution combustion method,
- electrospinning method,
- chemical precipitation method.

Each of these methods is associated with specific advantages and drawbacks, where a suitable synthesis route is selected based on the desired properties of the synthesized nanoparticles and the limitations of the available materials and technology. The sol-gel method is a relatively simple wet chemical method that is both economically feasible and efficient in producing high-purity nanoparticles, yet it requires a long processing time [75]. The hydrothermal/solvothermal method involves a hydrolysis reaction at elevated temperatures to obtain large crystals of high quality mainly when the synthesized material is unstable near the melting point. However, the disadvantage of this technique is that it involves the use of high-cost equipment [75]. Furthermore, the solution combustion method is a feasible and versatile technique usually employed in the preparation of oxides and contributes to the synthesis of high surface area powders. However, this method causes the agglomeration of powder particles, limiting the control over desired morphologies, and is associated with organic impurities resulting from incomplete combustion [76]. On the other hand, the electrospinning method is based on a novel technology that utilizes an electrostatic force to produce nanofibers allowing control over morphology, composition, and porosity. A Polyvinyl acetate solution (PVA) is prepared by dissolving a certain mass of PVA in distilled water under heat and magnetic stirring. Different concentrations of a magnesium nitrate precursor are added to the PVA solution, and the resultant mixture is electro-spun in a vertical electrospinning apparatus [77]. The synthesis route chosen in this work is chemical precipitation because it allows for effective V-doping with a high dispersion of dopant along the material surface, high final surface area to volume ratio, as well as owing to its simplicity, low-cost, and eco-friendliness.

3.1. Chemical Precipitation of MgO:V_x

In this work, V-doped MgO nanoparticles (MgO:V_x) were synthesized through chemical precipitation using magnesium nitrate (MgNO₃ · 6H₂O) as a magnesium source, sodium metavanadate (NaVO₃) as a dopant (0 mol%, 0.2 mol%, 0.5 mol%, and 0.7 mol%) and sodium hydroxide as a base. A typical synthesis procedure was employed to synthesize the V-doped MgO samples, for which 2 g of (MgNO₃ · 6H₂O) and different mol% of NaVO₃ (0 mol%, 0.2 mol%, 0.5 mol%, and 0.7 mol%) were dissolved in 100 ml of deionized water. A 4 M sodium hydroxide solution (NaOH) was added dropwise to the prepared magnesium nitrate solution until pH 12 was reached while stirring it continuously. The solution was kept under magnetic stirring for 2 h. The precipitate was filtered and washed several times using distilled water and ethanol. The final product was kept overnight in a hot air oven at 65 °C for drying and removing moisture. Finally, the obtained samples were treated for 2 h at 450 °C in a furnace, at a 5 °C/min heating rate, to obtain MgO:V nanoparticles. A schematic diagram of the synthesis route is shown in Figure 6. In later chapters, the samples will be abbreviated with MgO:V_x, where x represents the vanadium concentration in mol%.

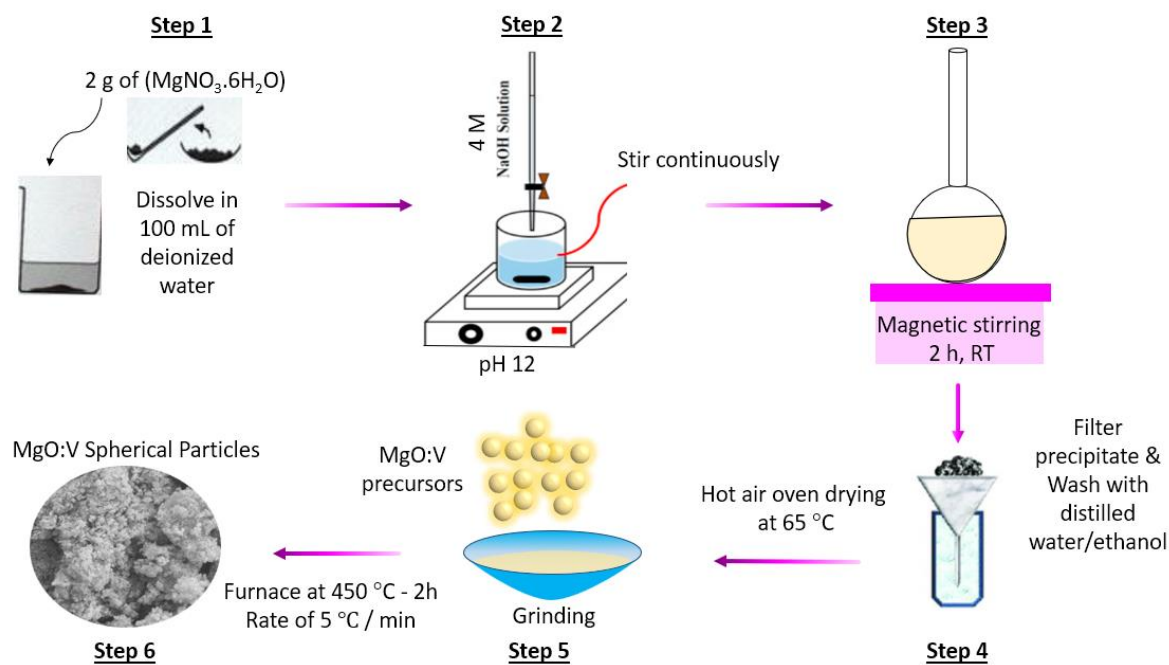


Figure 6: A schematic diagram of the chosen chemical precipitation synthesis method.

Detailed information regarding the chemicals used in the synthesis procedure is displayed below in Table 1. A summary of the notations used to describe the samples throughout the thesis is presented in Table 2.

Table 1: Detailed information about the chemicals used in the precipitation synthesis of MgO:V_x.

Chemical Formula	Compound Name	CAS No.	Supplier	Molecular Weight (g/mol)
MgNO ₃ .6H ₂ O	Magnesium Nitrate Hexahydrate	13446-18-9	Sigma Aldrich	256.41
NaVO ₃	Sodium Metavanadate	13718-26-8	Sigma Aldrich	121.93
NaOH	Sodium Hydroxide	1310-73-2	Sigma Aldrich	40.00
C ₂ H ₆ O	Ethanol	64-17-5	Sigma Aldrich	46.07

Table 2: Definition and description of the notations used to describe the MgO:V_x samples.

Sample Notation (MgO:V _x)	Sample Description
(Undoped) MgO	Pure magnesium oxide with no vanadium doping.
MgO:V0.2	Magnesium oxide doped with 0.2 mol% vanadium.
MgO:V0.5	Magnesium oxide doped with 0.5 mol% vanadium.
MgO:V0.7	Magnesium oxide doped with 0.7 mol% vanadium.

4. Characterization Methods

4.1. X-Ray Diffraction (XRD)

XRD is a non-destructive characterization technique utilized in analyzing the morphologies, identifying the phases, and providing the unit cell dimensions of several types of crystalline solid materials based on constructive interferences. The material is irradiated with an incident X-ray, where the intensities and scattering angles of the diffracted rays are measured when the conditions satisfy Bragg's Law. Prior to that the analyzed sample should be prepared by fine grinding and homogenization, where the composition of the average bulk is identified. Crystalline substances were revealed to act as three-dimensional diffraction gratings when exposed to X-ray waves as discovered by Max Von Laue in 1912 [78]. From that point on XRD became one of the most fundamental tools used in environmental, material, geological, and biochemical sciences to analyze crystal structures and atomic spacing. An XRD diffractometer comprises of three main components: the cathode ray tube, a sample holder, and a detector. Firstly, the cathode ray tube produces x-rays, filtered to monochromatic radiation, and concentrated on the tested sample. The rays interact with the sample, and when electrons acquire the minimal energy required to knock off inner shell electrons from the sample, Bragg's condition ($n \lambda = 2 d \sin \theta$) is satisfied with constructive interferences leading to the formation of characteristic x-ray spectra. Bragg's Law encompasses significant parameters, such as the radiation wavelength, the lattice spacing, and the diffraction angle. The diffracted rays are detected, processed, and counted, where an analogy between the signal peaks and lattice spacings enables the identification of an unknown material [78].

The crystal structure of the MgO:Vx samples was tested using a Bruker D2 Phaser diffractometer. The diffractometer utilizes a Cu-K α radiation source with a wavelength of $\lambda = 0.154$ nm in the $2\theta^\circ$ range between 10° to 90° at room temperature. The obtained results were used to calculate the average crystalline size using both the Scherrer equation and Williamson-Hall plots. A Rietveld refinement was conducted to further investigate the effect of doping on the lattice parameters of the crystal solid.

4.2. Raman Spectroscopy

Raman spectroscopy is a spectroscopic method that relies on light-matter interactions and polarizability alterations in the state of a molecule during its vibrational motion. In working principle, this technique utilizes scattering of light to measure the vibrational energy states of a sample. In 1928, Indian Physicist C. V. Raman first observed the Raman scattering phenomenon along with his research colleague K. S. Krishnan [79]. Following this discovery, Raman spectroscopy became a prominent methodology for inducing valuable chemical and morphological information about materials by means of identifying substances through their Raman fingerprint signal. As a molecule scatters light, a photon polarizes the electron cloud promoting it to a high-energy, unstable, virtual state, before directly reemitting the photon with different intensities and in different directions. Rayleigh scattering dominates this process, where the molecule's energy does not change, and scattered photons have equal wavelengths to the incident photons. In some rare cases, the scattering is inelastic, and some energy is transferred between the molecule and the photon, leading to what is known as Raman Scattering. In Stokes Scattering, the molecules acquire energy from the photon during the process, unlike the photon that loses energy when scattered. In Anti-Stokes Scattering, the opposite is true, as molecules relax to lower vibrational states by losing energy. It is expected that the probability of Stoke lines occurring is much higher than that of Anti-Stoke lines since the concentration of molecules in the ground state exceeds that of excited molecules. Consequently, Raman Spectroscopy is almost always involved with measurements related to Stokes Raman Shifts [79].

In 1948, Sir Chandrasekhara Raman stated that MgO “should prove a perfect choice to demonstrate by its spectral behavior” since the atomic vibration frequencies of the crystals occupying the cubic system display a unique monochromatic character [80]. Sir Raman further hypothesized that the Raman spectrum of MgO should resemble that of sodium chloride with an inverted symmetry. To complement the XRD analysis, the phononic mode changes that may occur in the MgO structure owing to the V-sites when doped were probed by Raman spectroscopy.

In this thesis, the Raman measurements were performed using an InVia Raman Spectrometer (Renishaw, UK) coupled with an upright microscope and a 532 nm frequency-doubled Nd:YAG solid-phase laser with maximum power at the sample surface.

4.3. Scanning Transmission Electron Microscopy (STEM)

The first person to build a STEM device was Baron Manfred von Ardenne, who was working for Siemens in Germany in the year 1938 [81]. The imaging results were of poor quality as compared to the ones possible nowadays because von Ardenne developed the device for a short duration before it was destroyed in a raid during the events of World War II. Thirty years later, the method was further enhanced with the design of a field emission gun and high-quality lenses to build the modern STEM device. In the 1990s, STEM technology was developed to enable imaging with 2 Å resolution, which would allow visuals of atomic structures in certain materials. A typical STEM consists of scanning coils, detectors, and circuit equipment allowing for an operational transition between STEM and Conventional Transmission Electron Microscopy (CTEM). The working principle is based on a beam of electrons focused by an optical lens to create a tiny probe that illuminates across the sample. The tested material is made as thin as possible to allow for maximum number of electrons to be transmitted, and ultimately for more scattered electrons to be detected. The intensity of each corresponding position as the microscope scans through the materials creates high-quality images [81].

The identification of the crystalline morphology of the synthesized MgO:V_x samples was accomplished using scanning transmission electron microscopy (STEM). STEM measurements were carried out on a Hitachi HD-2700 at a 200 kV electron acceleration, coupled with a double EDS detector (Oxford Instruments, Oxford, UK, AZtecSoftware, version 3.3). The samples were deposited on a 300-mesh copper electrolytic grid, to which a carbon film was attached. The sample was cleaned before being introduced into the electron microscope with a TEM ZONE, which removes unattached parts of the sample from the grid.

4.4. Electron Paramagnetic Resonance (EPR) Spectroscopy

EPR spectroscopy, otherwise known as Electron Spin Resonance (ESR), is a powerful tool employed in species depicting paramagnetic behavior, such as radicals, in order to acquire a better understanding of the extrinsic defects introduced to the crystal structure by doping. In 1944 Soviet physicist Yevgeny Zavoisky first explored EPR at Kazan State University. During the same period, British physicist Brebis Bleaney further developed the technique at the University of Oxford [82]. From that point on, EPR studies have been developed drastically, making this technology prominent in detecting and characterizing crucial processes such as polymerization, redox, and catalyzed reactions in a wide array of disciplines including but not limited to the natural, materials, and medical sciences. EPR is remarkably similar to Nuclear Magnetic Resonance (NMR) in working principle, with the exception that EPR utilizes microwaves instead of radio waves to investigate the interaction of an applied magnetic field with unpaired electrons instead of nuclei. According to the Zeeman Effect, or Zeeman Splitting phenomenon, in the presence of an external magnetic field, unpaired electrons either align their orientations with or against the field, creating in the process two spin states with an energy difference ΔE . The resonance condition is achieved when:

$$\Delta E = h \nu = g \beta B_0 \quad [1]$$

where h is Planck's constant ($6.626 \times 10^{-34} \text{ J}\cdot\text{s}^{-1}$), ν is the frequency of radiation (s^{-1}), g is the g -factor (2.0023 for a free electron), which is a unitless measurement of the intrinsic magnetic moment of the electron and holds as a distinct fingerprint of the material, β is the Bohr magneton ($9.274 \times 10^{-24} \text{ J}\cdot\text{T}^{-1}$), and B_0 is the applied magnetic field (T). Depending on the strength of the applied magnetic field (commonly lying in the microwave region – 9.5 GHz (X-band) & 35 GHz (Q-band)), a certain radiation frequency is needed to spur the excitation between the spin energy level. The spectrum generated from EPR exhibits two significant properties: the Proportionality Factor (g), and Hyperfine Interactions. The g factor generates valuable information about the electronic structure of a paramagnetic center by measuring the total magnetic moment, considering not only the effect of the device's applied magnetic field but also the influence of neighboring atoms/molecules with their distinct magnetic moments. Hyperfine Interactions, on the other hand, involve interactions between the unpaired electron(s) and the magnetic moment

of surrounding nuclei, leading to crucial information such as the number/identity of atoms in the examined species, as well as their relative distances from the unpaired electron [82].

EPR spectroscopy was performed on a CW EPR dual-band X and Q-band spectrometer Bruker ELEXSYS E500. The X-band measurements were carried out with an X-SHQ 4119HS-W1 Bruker microwave resonator working at a 9.63 GHz frequency and a 2 G modulation amplitude. An ER 5106 QT standard Bruker Q-band microwave resonator operating at 33.3965 GHz was employed for the Q-band measurements. Furthermore, to create the Aniso-Spin simulations, X-band EPR measurements were conducted using a Bruker EMX Nano device, as shown in Figure 7, at room temperature with a 9.63 GHz microwave frequency, a 3.162 mW microwave power, and a 2 G modulation amplitude with 50 scans.

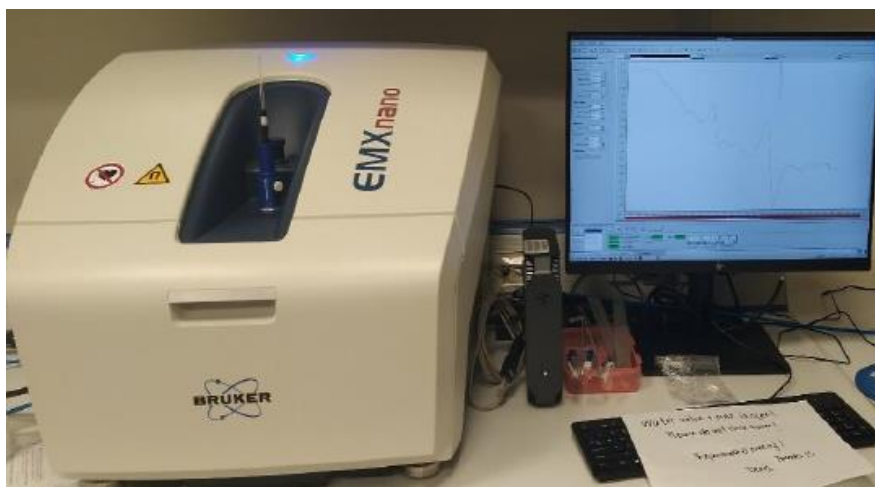


Figure 7: Bruker EMX Nano device utilized in EPR spectroscopy at Sabancı University (Location: FENS Lab 2110).

4.5. Photoluminescence (PL) Spectroscopy

PL spectroscopy is an optical-based, contactless, non-destructive method efficient for probing the electronic structure of materials and provides valuable information about the band gap energy, energy levels, and intrinsic/extrinsic defect-induced emissions. Photoexcitation occurs when a sample absorbs light energy and is excited to higher electronic states/energy levels. As

the material relaxes, electrons fall back to lower electronic states, releasing excess energy in the form of photons during the process. This emission of light or luminescence is referred to as photoluminescence. Typical applications of PL spectroscopy include understanding recombination mechanisms, investigating the substance quality, determining impurity concentration, detecting defects, and deciding on band gap energies [83].

The PL analysis of the samples was done using an FS5 Spectrofluorometer from Edinburgh Instruments. The measurements were conducted at room temperature with a 350 nm (3.54 eV) excitation wavelength, an excitation slit distance of 5 nm, and an emission slit distance of 10 nm.



Figure 8: Spectrofluorometer FS5 device utilized in PL spectroscopy at Sabancı University (Location: FENS Lab 2110).

4.6. Electrochemical (EC) Tests

The performance of the supercapacitors and the electrochemical performance of the electrode material was tested using CV, EIS, and GCPL. CV is a direct current (DC) technique that investigates the current response of a system to a series of potential steps to get a better understanding of the reaction kinetics and electrochemical behavior of the energy-storage device. On the other hand, EIS is an alternating current (AC) technique that studies the response of a system to sinusoidal fluctuations in current or potential as the system undergoes a frequency sweep from high range (MHz) to low range (mHz) frequencies. This is particularly crucial in

characterizing the electrochemical system in terms of its impedance, thus further analyzing the effective resistance of the device components towards an AC. GCPL explores the charging and discharging between two distinct potential points at a constant applied current to analyze the electrochemical stability, kinetics, and reversibility of the intercalation processes in the system [84].

Electrochemical (EC) measurements were performed using a Biologic VMP 300 multi-potentiostat with the standard two-electrode technique. The electrolyte used for all the test samples was 6 M KOH with glass fiber as a separator in a symmetric configuration design displayed in Figure 9. A potentiostat is required to conduct impedance tests in a linear regime so that the test results remain consistent throughout. CV curves were recorded in a voltage range of 0 to +1 V at different scan rates, with a standard scan rate for comparison of 50 mV/s. EIS results were obtained by applying a sinusoidal signal of 10 mV in a 10 mHz to 1 MHz frequency range. GCPL was conducted with a voltage window from 0 to +1 V at a specific current of 0.6 A/g (discharge current of 2.40 mA and a standard 4 mg sample mass).

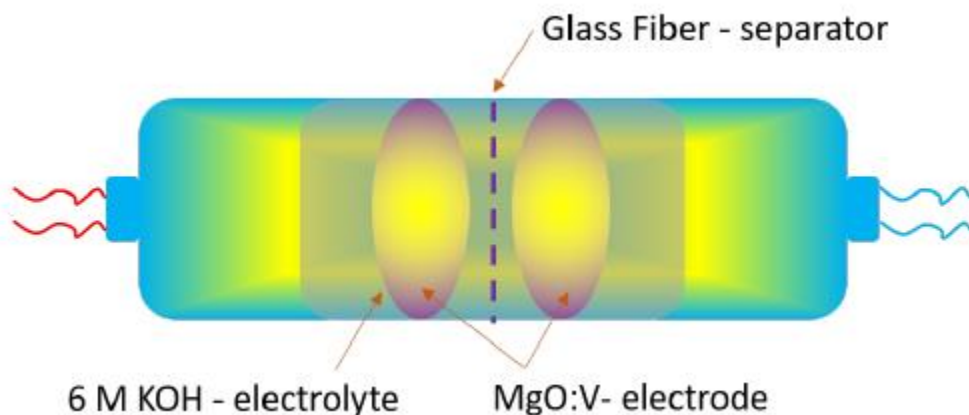


Figure 9: A schematic diagram of the tested symmetric supercapacitors constructed from the MgO:V_x samples.

5. Results & Discussion

5.1. X-Ray Diffraction Analysis

XRD measurements were carried out on the MgO:V_x samples, as illustrated in Figure 10, to evaluate changes in the crystalline plane and morphology before and after adding vanadium as a dopant in different mole percentages. The indexed diffraction peaks correspond to a typical rock-salt cubic MgO structure, otherwise referred to as Periclase [85]. Characteristic diffraction peaks of the undoped/V-doped MgO samples at diffraction angles of $2\theta = 37^\circ$, 42° , 62° , 76° , and 78° correlate to the expected orientation of the standard cubic structure of MgO along the planes (111), (200), (220), (311) and (222), respectively [86]. The first peak at 37° is associated with the (111) plane of magnesium hydroxide, whereas the following peaks outline the calcination of magnesium hydroxide to MgO [42].

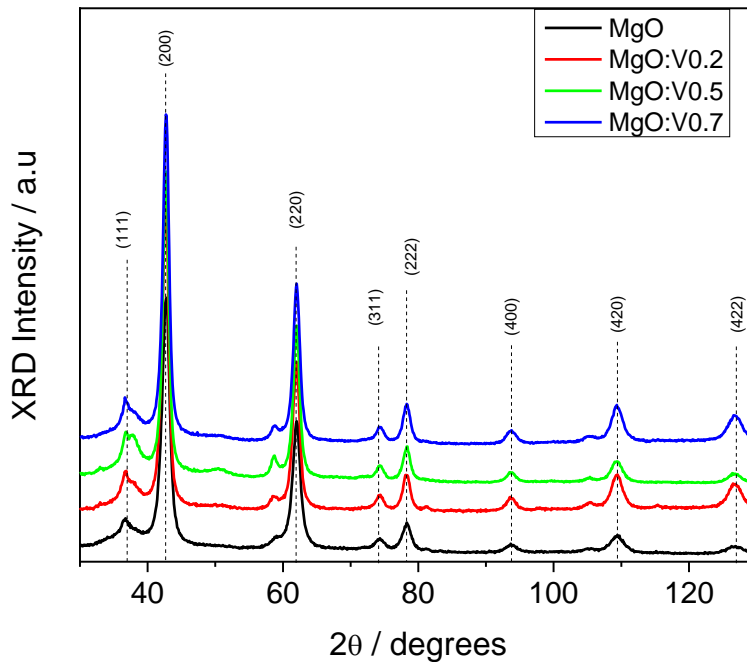


Figure 10: X-ray diffractogram of undoped MgO (black), MgO:V0.2 (red), MgO:V0.5 (green), and MgO:V0.7 (blue).

It is observed that the addition of V does not contribute to generating new peaks at different diffraction angles, implying that doping with this rare earth metal ion does not influence the crystal structure of MgO. Nonetheless, it is noticed that as the mole percentage of V dopant increases, the diffraction peak intensities increase accordingly, indicating higher levels of crystallinity due to the presence of V [87]. As described in literature, the effect of the crystallite size distribution can influence the surface compression of the crystal lattice, leading to a significant increase in the band gap, mass transport, and especially oxygen vacancies transport, directly influencing the electrochemical properties of the material [88, 89].

The Scherrer Equation and Williamson-Hall Plots were used to estimate the average crystallite size of the samples.

$$D = \frac{K\lambda}{\beta_D \cos\theta} \quad [2]$$

where D is the average crystallite size (nm), K is the shape factor determined by the lattice morphology (unitless), λ is the wavelength of the X-ray source (= 0.154 nm), β_D is a measure of peak broadening (radians), and θ is the angle associated with the diffraction peak (radians) [90].

Since The Scherrer Equation is only valid in the nanoscale, and only concerned with the broadening of peaks due to crystal size, disregarding broadening due to strain, Williamson Hall (W-H) plots are incorporated to investigate broadening due to the strain effect [90].

$$\beta_t = \beta_D + \beta_\varepsilon \quad [3]$$

$$\beta_D = \frac{K\lambda}{D \cos\theta} \quad [4]$$

$$\beta_\varepsilon = 4\varepsilon \tan\theta \quad [5]$$

Where β_t is the total broadening (radians), β_D is the broadening due to crystal size (radians), β_ε is the broadening due to strain (radians), and ε is the strain.

By rearranging the variables, with some mathematical manipulations, the final form of Equation 3 is linearized as shown below.

$$\beta_t \cos\theta = \frac{K\lambda}{D} + 4 \varepsilon \sin\theta \quad [6]$$

As can be noticed, the strain ε is related to the slope of the W-H plots, shown in Figures 11 & 12, when plotting $\beta_t \cos\theta$ versus $4 \sin\theta$, whereas the average crystallite size D (with consideration

of the strain effect) is calculated from the y-intercept. The difference between the average crystallite size D and the actual particle size should be highlighted. The average particle size should always be larger than the average crystallite size since a single particle can comprise of multiple agglomerated crystals. Further investigation of the average particle size will be demonstrated in STEM analysis in Chapter 5.3.

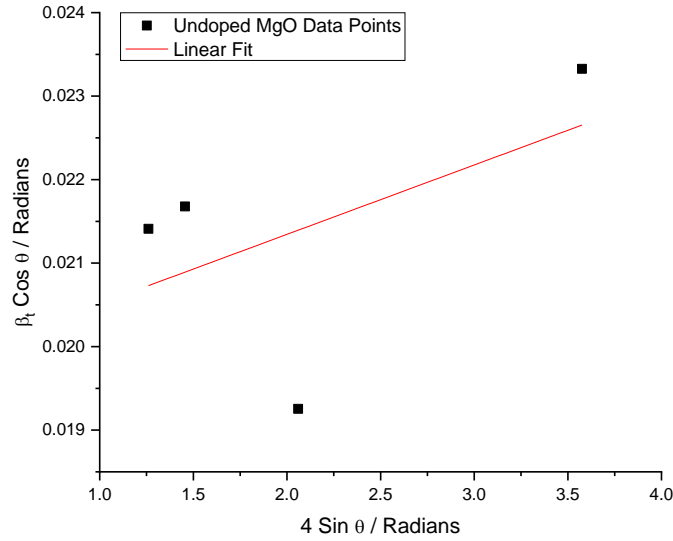


Figure 11: W-H plots for undoped MgO with a linear fit.

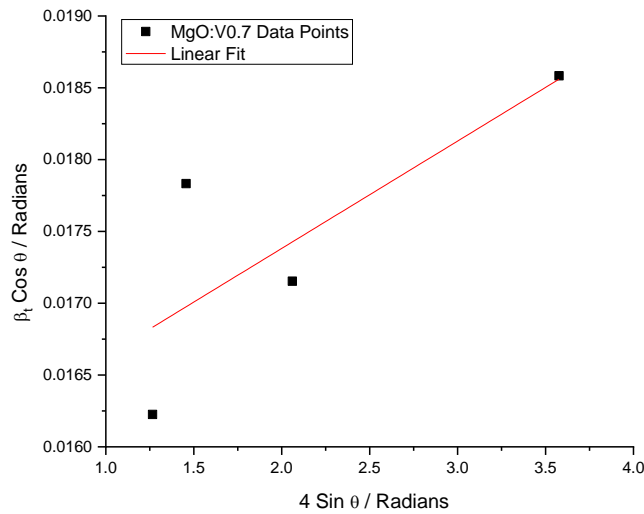


Figure 12: W-H plots of MgO:V0.7 with a linear fit.

The W-H plots revealed negative slopes for MgO:V0.2 and MgO:V0.5, whereas for MgO undoped and MgO:V0.7 the slopes were positive as illustrated in Figure 11 and Figure 12. Thus, this implies that the undoped MgO crystal structure exhibited the highest strain effect (with the largest slope value). Nonetheless, at small doping concentrations of 0.2 and 0.5 mol% V, the micro-strain effects were of no impact anymore as signified by the negative slope values. After a threshold doping percentage of 0.7 mol%, it was found that a higher concentration of V restores the micro-strains in the cubic MgO structure; however, the strain was found to be less than that in the original undoped MgO sample (smaller slope value). In Figure 13 below, the average crystallite size obtained from both The Scherrer equation and W-H plots is demonstrated. For MgO:V0.2 and MgO:V0.5, W-H plot results invalidated the average crystallite size calculated from The Scherrer equation. This is because it is always expected that the average crystallite size incorporating the strain effect (W-H plots) would be larger than that disregarding the strain effect (The Scherrer Equation), opposite to what is observed in the aforementioned samples.

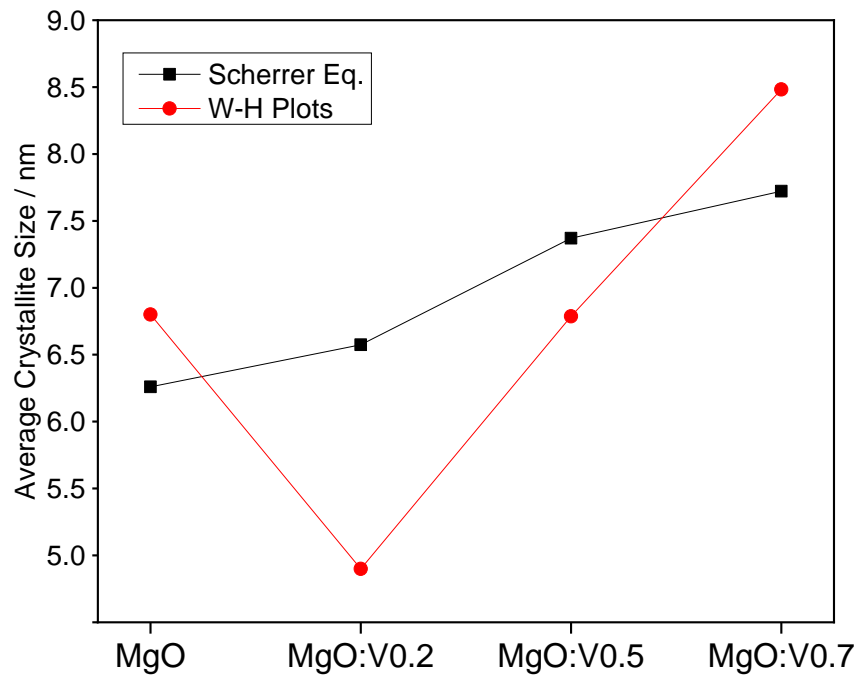


Figure 13: Average crystalline sizes (D) of the MgO:V_x samples calculated from The Scherrer Equation (Black) and W-H Plots (Red).

As the dopant concentration increases, the average crystallite size increases, as shown in Figure 13. Based on the difference between the ionic radius of Mg^{2+} (0.72 Å with a coordination number of VI in MgO) and V^{4+} (0.53 Å with a coordination number of V in VO^{2+}) [91], the formation of a single-phase doped oxide was expected, as the smaller V^{4+} cations participate in partial ion exchange and penetrate smoothly the MgO crystal lattice [92]. The existence of the V^{4+} ions is demonstrated in Chapter 5.4. The addition of V results in internal stresses in the cubic structure of MgO, and as the dopant mole percentage exceeds a certain threshold value, the strain increases, eventually leading to structural defects. Although some works by Letifi *et al.* [93] and Nourmohammadian *et al.* [94] report that adding V as a dopant reduces the average crystalline size, as V^{4+} ions substitute Mg^{2+} ions in the crystal, Figure 13 shows the opposite with increasing crystallite size. The increasing tendency is probably associated with the type of defects in the samples, where V^{4+} ions must penetrate the crystal lattice and fill in Mg^{2+} vacancies, thus increasing the crystal size. A similar result was reported by Aksay *et al.* [86], where it was found that doping MgO with 0.5, 1, and 3% of Al^{3+} increased the average crystallite size from 14.43 to 17.90 nm.

Furthermore, a Rietveld refinement was done for the XRD results obtained for the undoped and 0.7% doped MgO samples. The fit was performed with the CIF. file no. 1000053 with the $Fm\bar{3}m$ space group. The results are summarized in Table 3 and Figure 14 below.

Table 3: Lattice parameter, unit cell volume and occupancy of individual atoms in the structure.

Sample	Lattice Parameter “a” [Å]	Unit Cell Volume “V” [Å³]	Occupancy Mg : O : (V)
MgO Undoped	4.217	75	0.02 : 0.02
MgO:V0.7	4.217	75	0.02 : 0.02 : 0.0001

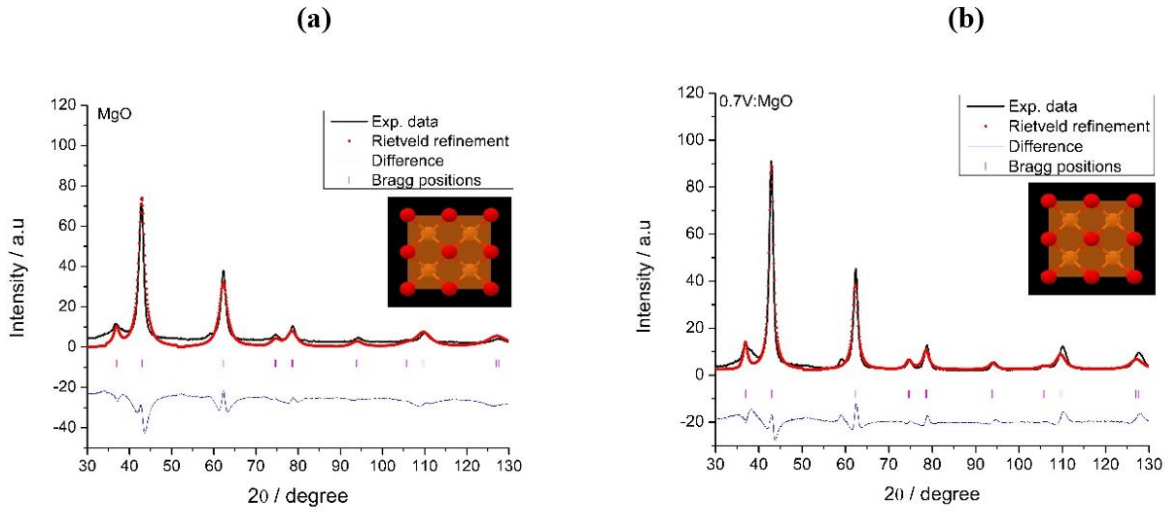


Figure 14: Rietveld refinement with discrepancy from experimental data and Bragg positions displayed for (a) MgO, and (b) MgO:V0.7.

Despite the fact that it has been seen in literature [95, 96] how doping can significantly affect the stoichiometry of a host material, the Rietveld refinement revealed that even at the highest vanadium doping concentration, the unit cell parameters ($a = b = c = 4.217 \text{ \AA}$ and $V = 75 \text{ \AA}^3$) were unaffected. Additionally, the occupancy obtained from the Rietveld refinement (0.02 : 0.02 : 0.0001), which is a measure of the presence of an atom at its mean position, shows a negligible change in the stoichiometry, indicating that the doping process did not affect the structure of the host MgO material. This can be justified by the small doping percentages utilized in this work.

5.2. Raman Analysis

Considering the high refractive index of MgO, Sir Raman first characterized the material in the form of thin flakes, utilizing long wavelength exciters; 4047 Å and 4358 Å of mercury. Consequently, the first Raman spectroscopy of MgO displayed two peaks corresponding to wavenumbers of 617 cm⁻¹ and 355 cm⁻¹ [80]. Later in 1985, Ishikawa *et al.* reported the first-order Raman scattering in MgO microcrystals with peaks generated at 280 cm⁻¹, 446 cm⁻¹, and 1088 cm⁻¹ (the strongest peak was at 446 cm⁻¹) [97]. Furthermore, Athar *et al.* found that the Raman spectrum of MgO displayed intense peaks at several regions in different bands, confirming the cubic structure with reference to the tangential modes of the material in the amorphous phase [98].

Although 14 different crystal structures have been revealed for VO₂, the most common is the monoclinic crystal VO₂ (M1). The lattice structure is tetragonal and rutile-like, contributing to several broad and weak lines. For VO₂ (M1), 18 Raman active vibrations exist; 9 A_g + 9 B_g [99]. Shvets *et al.* reported that while the A_g phonons were located at wavenumbers of 137, 194, 224, 310, 340, 393, 499, 612, and 663 cm⁻¹, the B_g phonons corresponded to wavenumbers of 143, 224, 262, 393, 442, 484, 582, and 820 cm⁻¹ with the 9th mode being missing but speculated to be at 450 cm⁻¹ [99]. Points of overlap between both phonons occurred near 224 cm⁻¹ and 393 cm⁻¹, although they have not been resolved experimentally.

Figure 14 shows the comparative Raman spectra of undoped and V-doped MgO samples. The alterations in the vibration bands in the range of 200 - 1400 cm⁻¹ are given. These peaks situated below 1500 cm⁻¹ correspond to the D-band, otherwise referred to as the breathing mode. To emphasize the effect of the presence of V in the structure, the undoped MgO spectrum normalized to the MgO:V0.7 spectrum is given in the inset of Figure 15. MgO exhibits a rock-salt structure indexed in the cubic Fm $\bar{3}$ m space group. The structure of MgO contains a basic unit of four atoms in the unit cell. Thus, the number of optical phonons is 9 (3 × LO, 6 × TO). According to the group theory, the possible Raman active modes of MgO are A_{1g}, E_g, and T_{2g} [100]. Therefore, the symmetrical stretching vibration band centered at 1085 cm⁻¹ can be ascribed to the TO-LO surface phonon modes in the MgO lattice. The band around 440 cm⁻¹ can be assigned to the E₂ double-degenerate vibration mode of MgO [97, 101]. The effect of the

presence of V in the structure on the phonon modes can be seen in Figure 15. The broad band at around 820 cm^{-1} might be attributed to the shorter symmetric V=O stretching mode (A_g), implying a local formation of vanadium oxide. To the best of knowledge, these peaks cannot be linked to the coexistence of VO_x along with MgO, i.e., whether or not vanadium fully dissolves in MgO. The asymmetric bending vibration was also detected at about 322 cm^{-1} as a weak shoulder [102, 103].

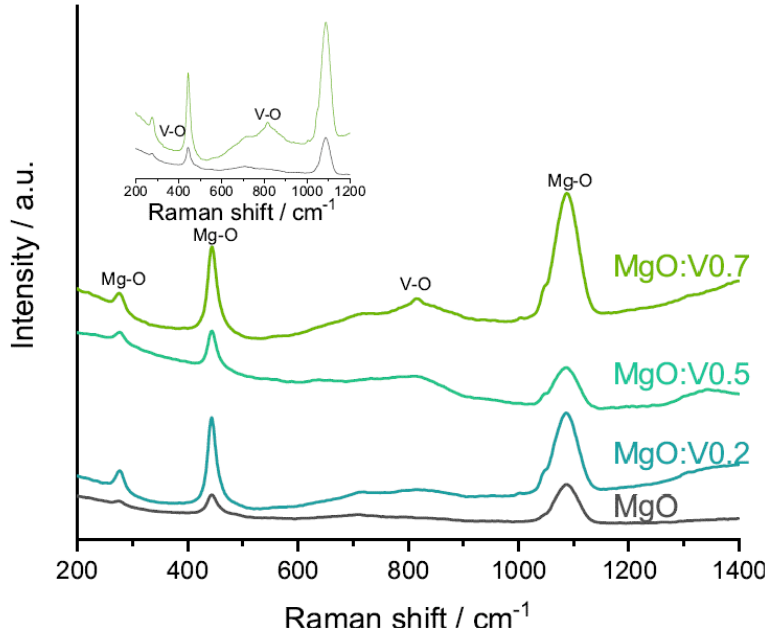


Figure 15: Raman spectra of undoped and V-doped MgO powder.

Since Raman spectroscopy did not strongly validate the existence of V in the crystal structure, the presence of the dopant element was confirmed by complementary Energy Dispersive X-Ray Spectroscopy (EDX) measurements for the MgO:V0.7 sample, presented in Figure 16. The EDS layered image and the elemental mapping images show the material's Mg, O, and V distributions. Even though the vanadium concentration used to dope the MgO sample was near the EDX detection limit, which generated artifacts in the detection of this element, it is observable that there is an agglomeration of detected vanadium signals at the MgO site, as best depicted by the mapping of the elements.

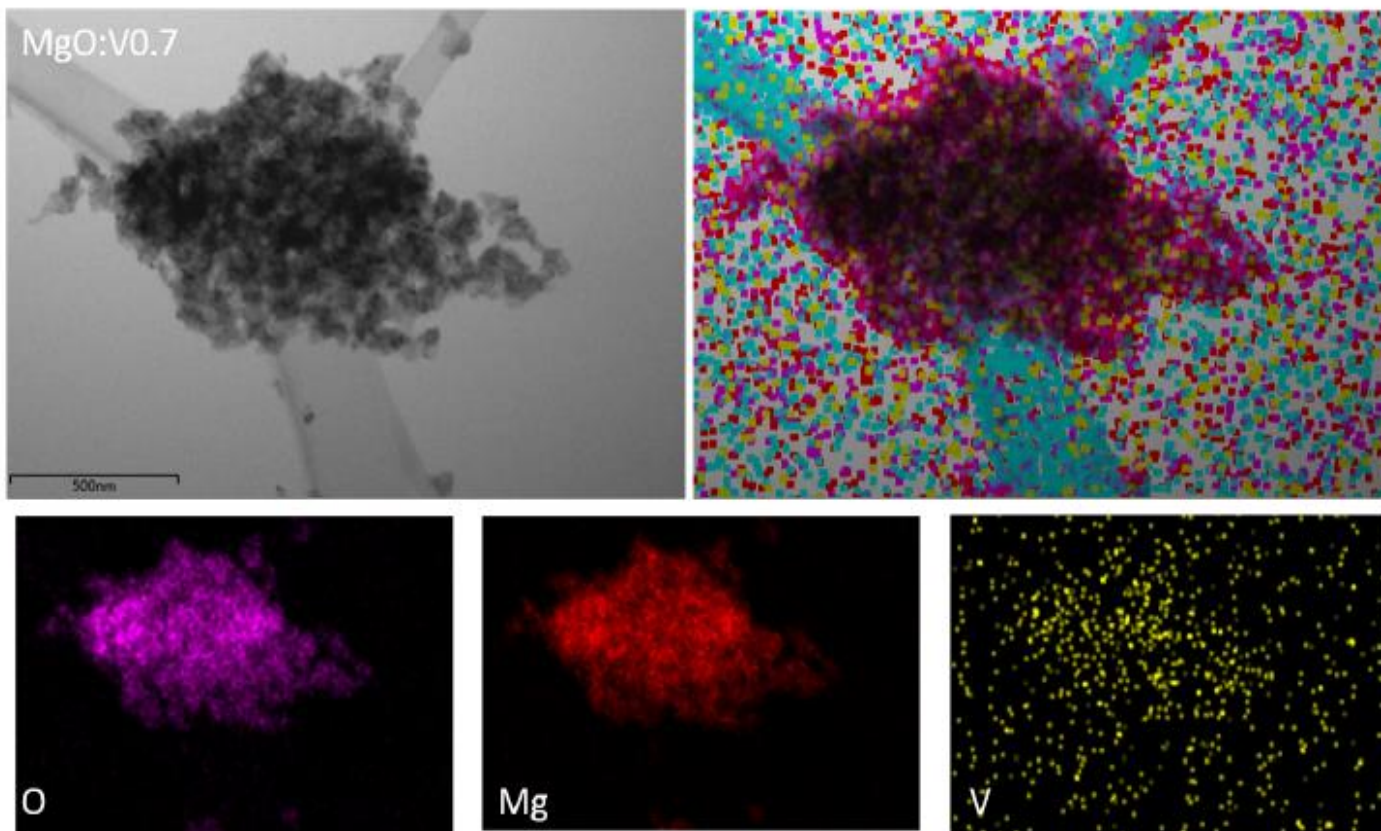
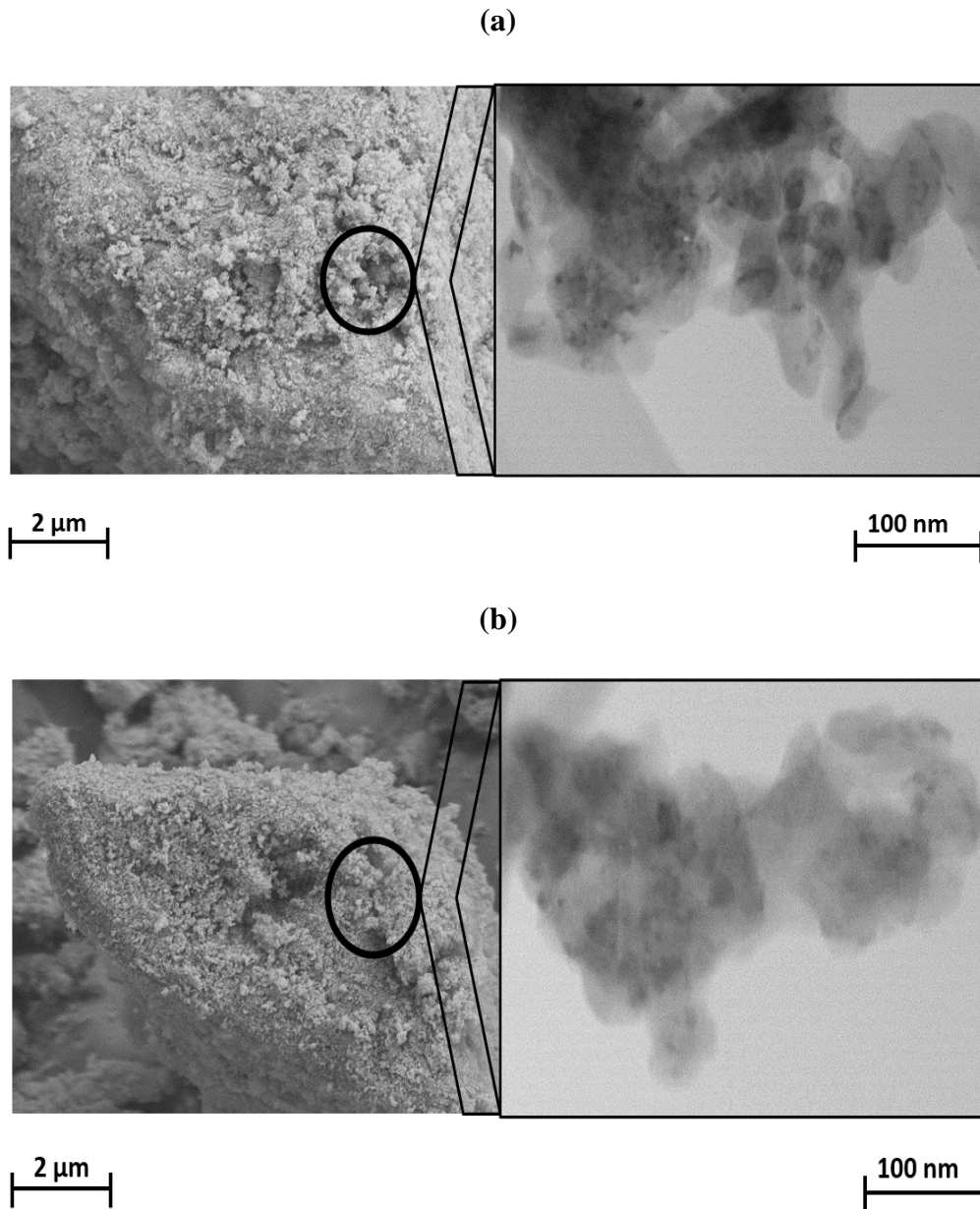


Figure 16: EDX and mapping images of the MgO:V0.7 sample showing the main elements O (purple) and Mg (red), as well as the dopant element V (yellow).

5.3. Scanning Transmission Electron Microscopy Analysis

The morphology and average particle size distributions of the MgO:V_x nanoparticles were further investigated and evidenced by STEM. Figure 17 illustrates the STEM images of all MgO:V_x samples at a scale of 2 μm, further magnified into a scale of 100 nm for average particle size analysis.



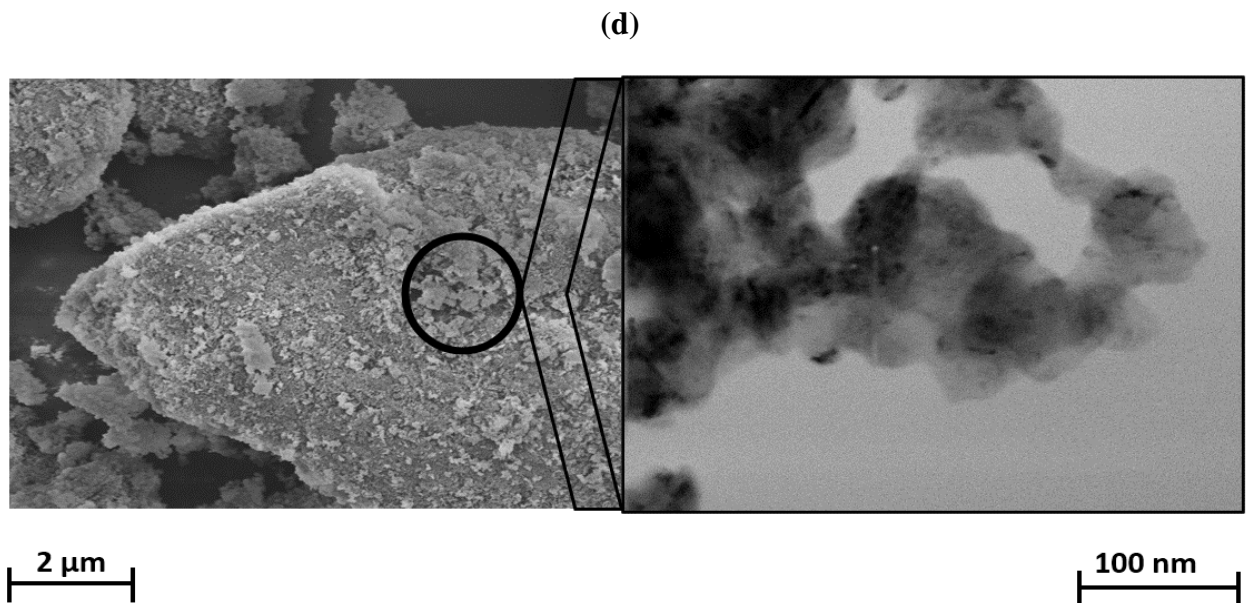
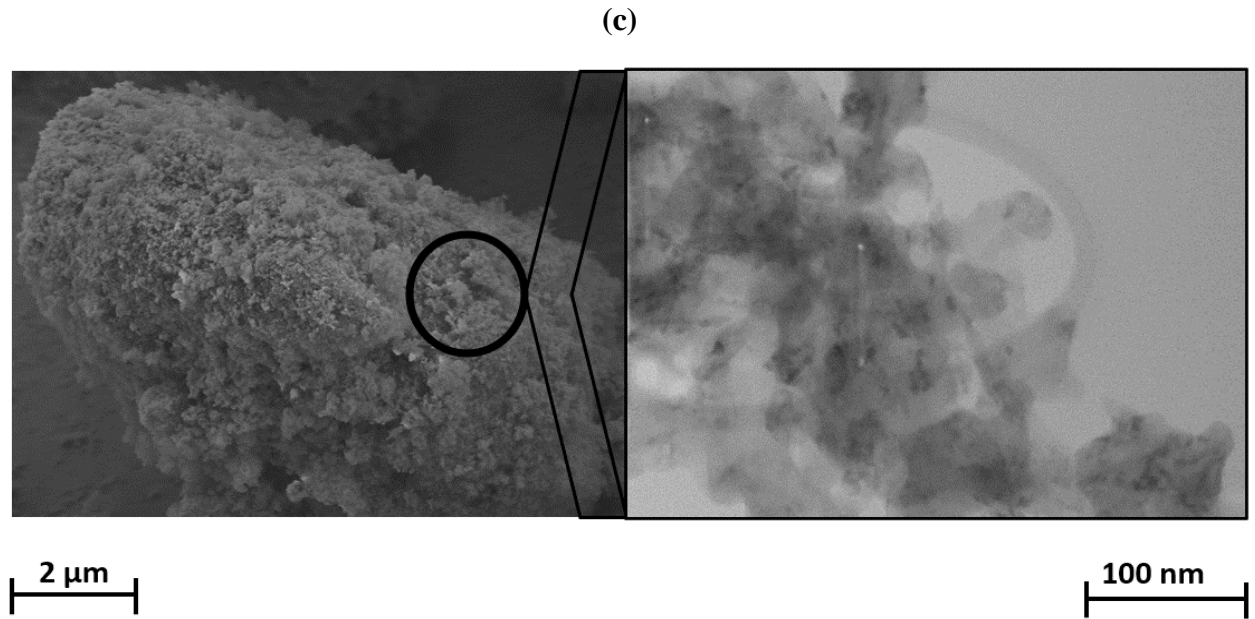


Figure 17: STEM Images of (a) Undoped MgO, (b) MgO:V0.2, (c) MgO:V0.5, and (d) MgO:V0.7.

The STEM images reveal the formation of almost polyhedral nanoparticles with a strong tendency to form clusters. This can be attributed to the selected synthesis method of co-precipitation, whereby insufficient heating leads to incomplete calcination, thus a greater presence of the precursor and a greater degree of irregularities in the final morphology. Although

it has been found in literature that pure MgO nanoparticles characterized with SEM displayed a combination of nanosphere and nanorod-shaped structures, this was correlated to the sol-gel synthesis method, and the morphology was said to be influenced by the presence of ionic liquids [42]. Furthermore, Patil *et al.* reported the morphology of V-doped magnesium hydroxide (3.9, 5.1, and 6.0 wt%) before and after calcination [42]. They affirmed that the majority of the particles were agglomerated, forming fused masses at random sites, similar to our case. The particles were compact, and voids were only formed upon heating to 400 °C for a duration of 4 hrs. After calcination, V-doped MgO nanoparticles were formed with a more evident porous network. They deduced that the particle sizes dropped from values greater than 200 nm before calcination to particle sizes less than 80 nm after calcination [42].

ImageJ software was utilized to further analyze the STEM images of the undoped MgO and the MgO:V0.7 samples with a 100 nm scale. Histograms were created to illustrate the count or frequency of particles exhibiting the corresponding average particle sizes in the analyzed images. A Gaussian curve was fitted for the undoped MgO, whereas a log-normal distribution was fitted for MgO:V0.7 to calculate the average particle size of each sample. The graphs are shown below in Figure 18.

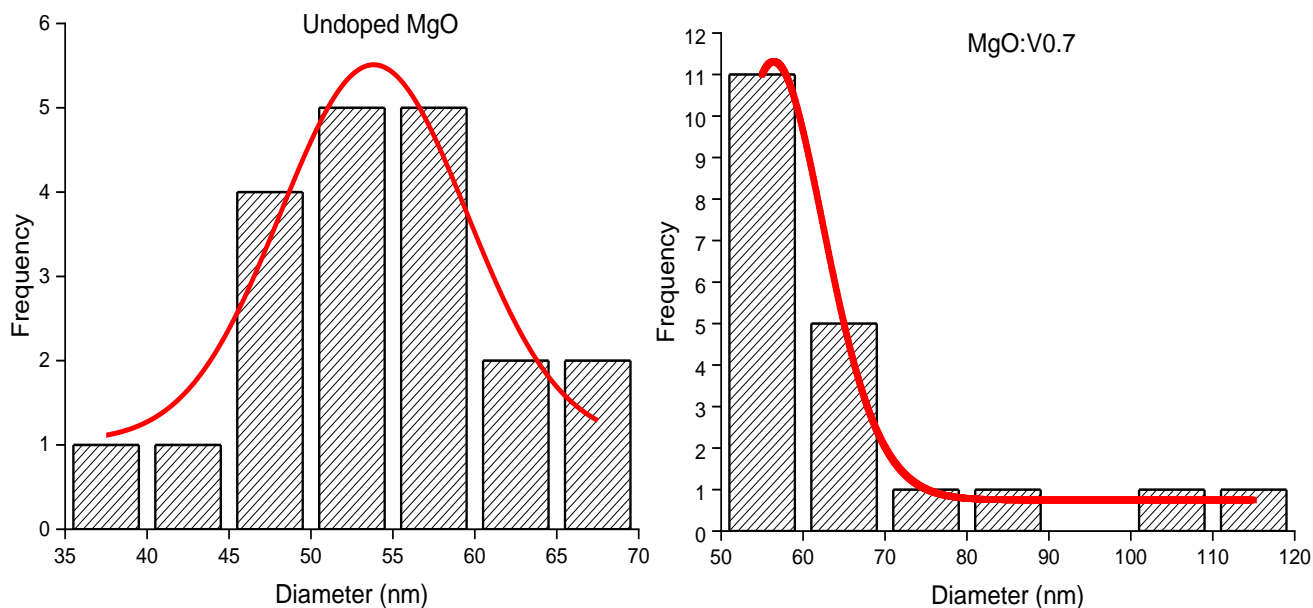


Figure 18: Histograms fitted with a Gaussian curve (left) and log-normal distribution (right) to calculate the average particle sizes of undoped MgO and MgO:V0.7.

The undoped MgO sample was found to exhibit an average particle size of $(54 \text{ nm} \pm 2 \text{ nm})$, whereas MgO:V0.7 was revealed to possess an average particle size of $(57 \text{ nm} \pm 2 \text{ nm})$. It was expected that the average particle sizes via STEM would be greater than the average crystalline sizes via XRD illustrated in Figure 13. This is because as mentioned earlier in Chapter 5.1, a particle can comprise of many crystals structured in an extended network involving pores. According to Figure 13, the average crystalline size of undoped MgO was 6.5 nm, and that of MgO:V0.7 was 7.9 nm. With STEM analysis, Figure 18 firstly confirmed the prediction of an average particle size greater than the average crystallite size for both samples, secondly verified the increase in particle diameter with doping, and thirdly complied with literature where 40 – 80 nm V-doped MgO nanorods/nanospheres were reported [42].

5.4. Electron Paramagnetic Resonance Analysis

As mentioned before in Chapter 2.2, MgO crystallizes to form a Halite or a rock-salt cubic structure with an octahedral coordination geometry of Mg^{2+} and O^{2-} , where each Mg atom exhibits a coordination number of six (with neighboring oxygen atoms) in the bulk. In literature, the following defects have been reported to exist in the MgO structure [61]:

- Anionic vacancies: these include oxygen vacancies denoted with colored F-type centers, and their clusters denoted with colored F_2 -type centers. They mostly exist as neutral or single anionic vacancies.
e.g., F, F^+ , F^{2+} , F_2^{2+} , F_2^+ , and F_2^{3+} .
- Cationic vacancies: these include magnesium vacancies denoted with V.
e.g., V_{Mg}^0 , $\text{V}_{\text{Mg}}^{1-}$, and $\text{V}_{\text{Mg}}^{2-}$.
- Interstitial defects: these are point defects where oxygen occupies interstitial sites in the crystal structure and are denoted with O_i .
e.g., O_i^0 , O_i^{1-} , and O_i^{2-} .
- Schottky defects: these are point defects and involve a cation and an anion leaving their original sites.
e.g., $\text{V}_{\text{Mg}}^0 + \text{F}$

Figure 19 below illustrates an MgO supercell comprising 64 atoms, with possible sites for lattice vacancies indicated in the diagram.

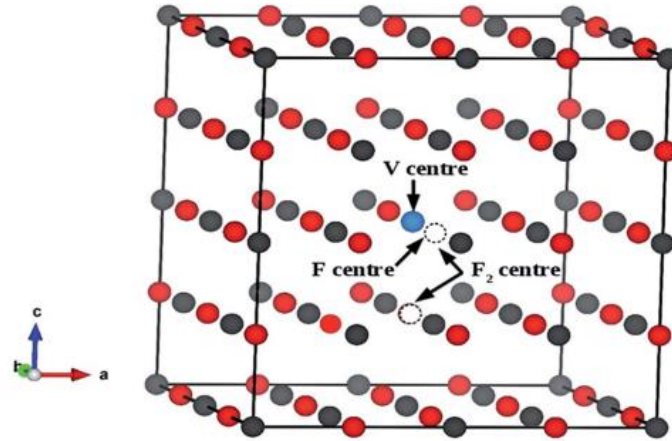


Figure 19: Diagram of a MgO supercell. Red: O ions, Black: Mg ions, Blue: Mg vacancy, Empty Dotted Spheres: O vacancy. Adapted from [61].

X-band EPR measurements, shown in Figure 20, revealed that the undoped MgO sample presented two EPR signals that are overlapping. In contrast, the V-doped MgO samples show a complex EPR signal with eight hyperfine lines characteristic to V^{4+} paramagnetic ions. Since the same quantity of sample was used, a direct comparison of the EPR signal intensities is possible, revealing an increasing linear tendency, which indicates that the concentration of V^{4+} dopant ions increases linearly as expected.

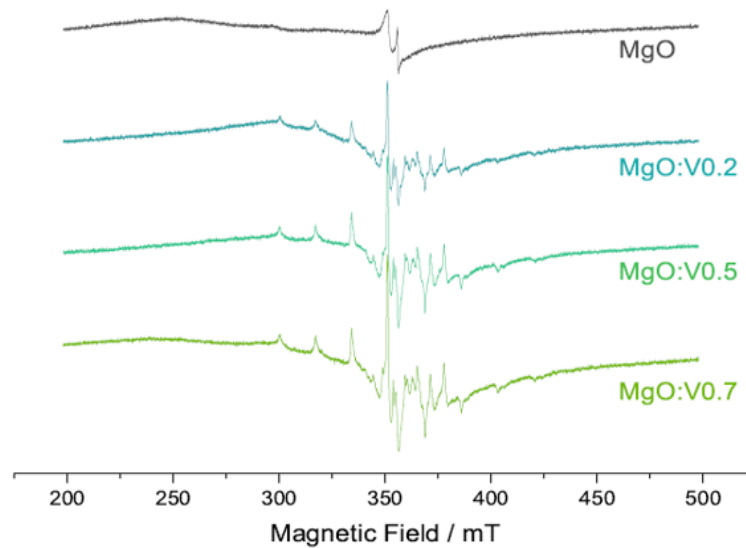


Figure 20: X-band EPR spectra of the MgO:V_x samples.

The undoped MgO presented two EPR signals (at a magnetic field value of approximately 350 mT), an axial one with $g_{\parallel} = 2.0032$ and $g_{\perp} = 2.0001$, and an anisotropic one with $g_{\text{iso}} = 1.97866$. The first signal with characteristic g matrix components has been attributed to oxygen vacancy F-centers (designated in the following as hole centers). The second signal feature with the g value slightly smaller than the free electron spin value has been attributed to electrons trapped at the material's surface [104]. In fact, Pathak *et al.* confirmed the presence of four distinct signals for the MgO structure at $g = 2.07$ (S_{I}), 2.03 (S_{II}), 1.98 (S_{III}), and 1.96 (S_{IV}) [62]. Broad peaks at S_{I} and S_{II} were attributed to the strong coupling of electron spins in the system, and the tendency to produce a cluster of spins. The S_{I} signal was correlated to trapped holes at Mg vacancies that create paramagnetic species (EPR active), whereas the S_{II} signal was linked with F^+ centers. On the other hand, the S_{III} and S_{IV} signals were attributed to trapped superoxide radicals. Both EPR MgO-based signals, denoted by the pink vertical lines in Figure 21 and confirming the results of Pathak *et al.*, are present in all V^{4+} doped samples, indicating that they do not interact with the dopant element.

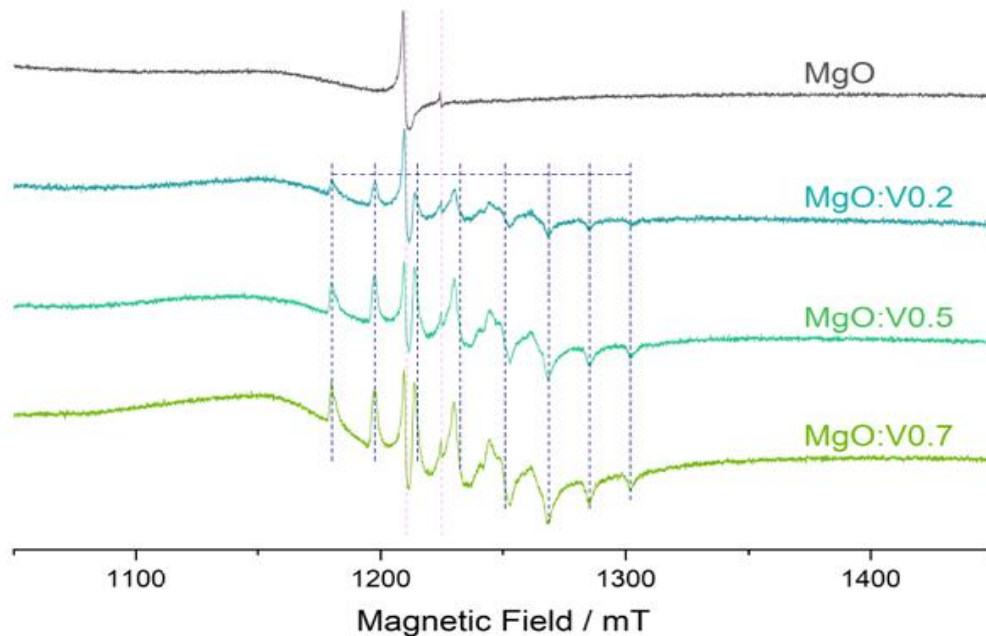


Figure 21: Q-band EPR spectra of the $\text{MgO}:\text{V}_x$ samples. The pink dashed lines portray MgO intrinsic defects, whereas the purple dashed lines show the well-resolved hyperfine lines due to the V^{4+} ions.

The V-doped MgO samples present, as observed in the X-band measurements, an eight-line hyperfine splitting structure (purple lines), attributed to the strongly localized 3d electrons of the V^{4+} ion, which interact with only one vanadium nucleus. The nature of the EPR signals observed in the X-band was further investigated using Q-band measurements, as presented in Figure 21, to reveal anisotropies and better separate overlapping EPR signals. Using the experimental microwave frequency of 33.925 GHz, a g-value of 1.97 was calculated, similar to other values reported in the literature for vanadium-based compounds with an (IV) oxidation state [105]. Since the V^{4+} ion has an electronic spin $S = 1/2$, and the nuclear spin for the ^{51}V isotope (with a natural abundance of 99.5%) is $I = 7/2$, the isotropic EPR spectrum of isolated V^{4+} species consists of a set of eight hyperfine lines ($2I + 1$) due to the dipole-dipole interaction between the magnetic moment of the ^{51}V nucleus and the electronic moment of the unpaired V^{4+} electron [106].

Furthermore, Aniso-Spin curves were automatically fitted for all samples tested in the X-band with 50 scans at a power of 3.162 mW (attenuation of 15 dB) as seen in Figure 22. The Aniso-Spin fits successfully simulated the sharpest signal attributed to the F/F_2 -type intrinsic defects, which correlate to the g-factor of 2.0032.

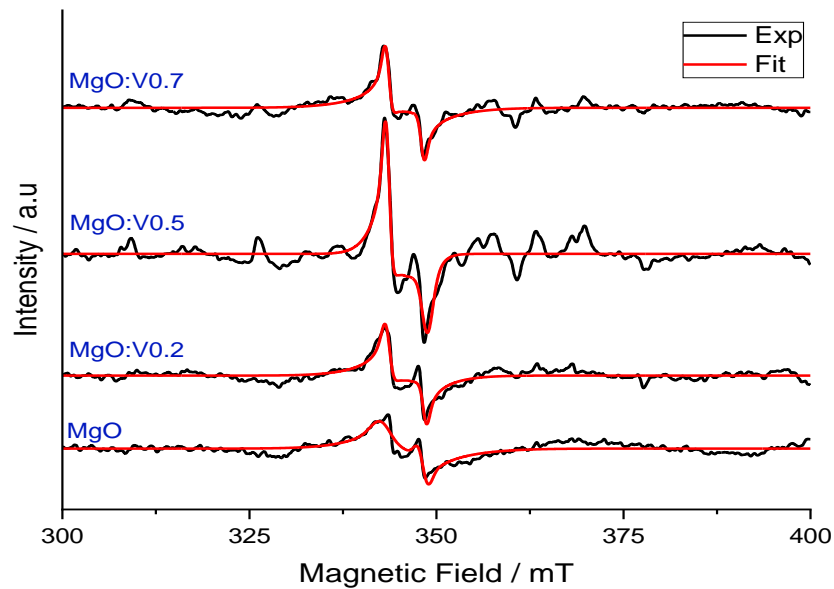


Figure 22: X-band Aniso-Spin fits of the MgO:V_x samples (50 scans at a power of 3.162 mW).

With the aid of the Aniso-Spin simulation program, a report involving the electron spin density, total spin angular momentum, and total number of spins is generated. Figure 23 below displays the effect of V-doping on the electron spin density at a corresponding g-factor of 2.0032.

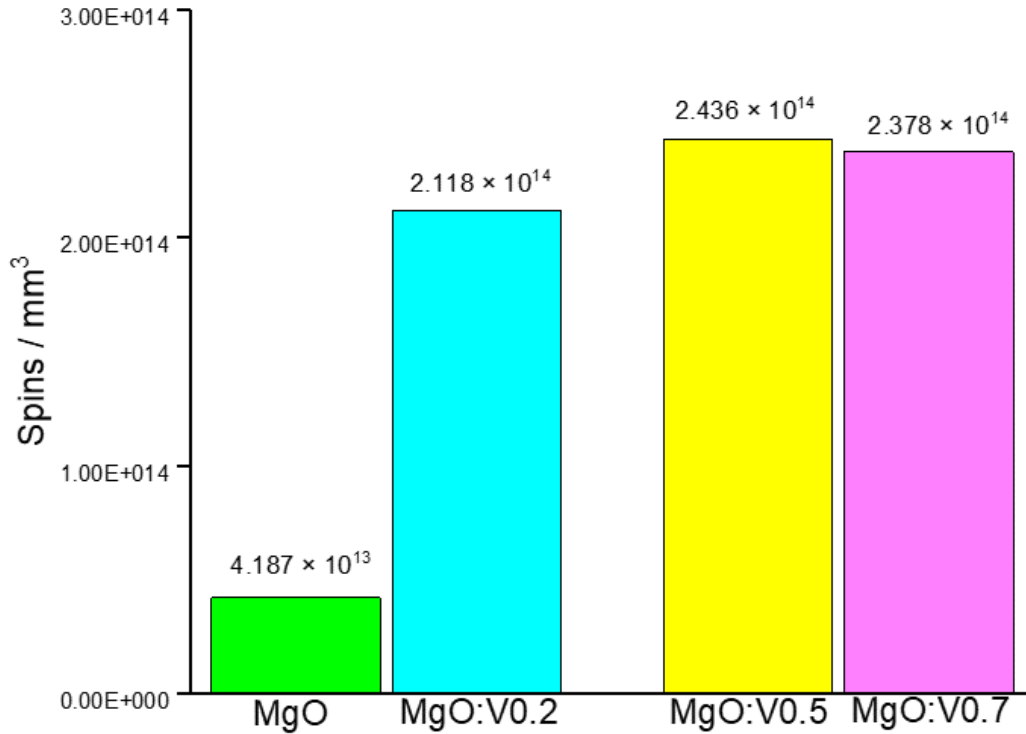


Figure 23: The electron spin density of the MgO:V_x samples.

It can be clearly seen that the MgO:V0.7 sample has an electron spin density (2.378×10^{14} spins/mm³) five times greater than that of the undoped MgO sample (4.187×10^{13} spins/mm³). This higher electron spin density reveals that doping with V promotes a greater activity of paramagnetic centers and free electrons, thus increasing even the intensity of the intrinsic defects at the 2.0032 g-factor (peaks become sharper). This electronic activity will be further illustrated and discussed in PL analysis in Chapter 5.5, and eventually, the impact of this higher electron spin density on the electrochemical performance of the constructed supercapacitors will be highlighted in Chapter 5.6.

5.5 Photoluminescence Analysis

The optical properties of the undoped and V-doped MgO samples were analyzed utilizing PL spectroscopy. Unlike EPR spectroscopy, which is only sensitive to paramagnetic species, PL spectroscopy provides sensitivity towards all types of defects, thus allowing the detection of a wider range of intrinsic and extrinsic structural defects. Figure 24 below shows the PL emission spectra of the undoped and V-doped MgO samples at room temperature with a 350 nm (3.54 eV) excitation wavelength and an emission slit distance of 10 nm.

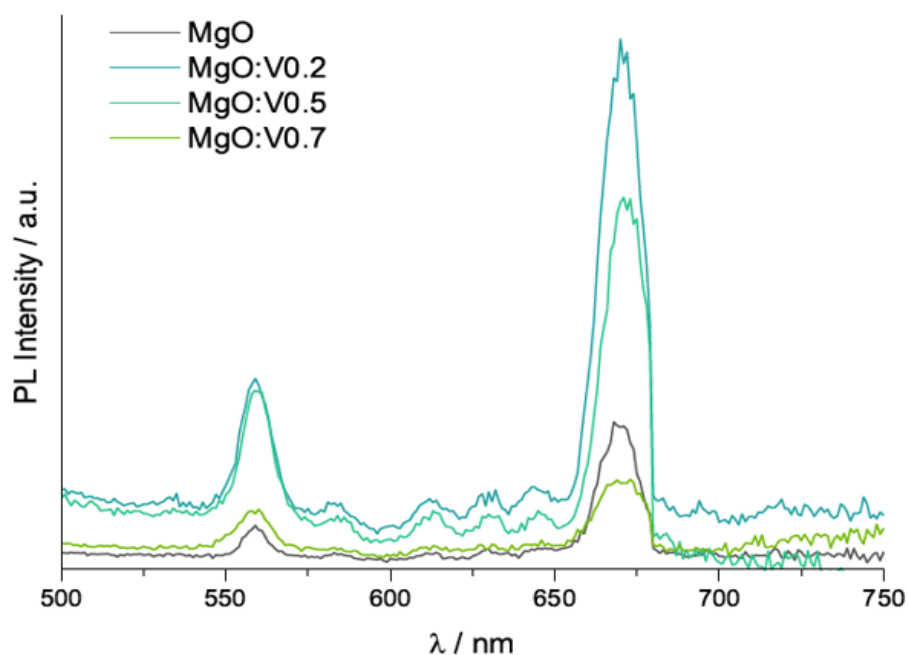


Figure 24: PL spectra of the MgO:V_x samples.

As reported in previous studies, MgO has a band gap energy between 4.2 - 7.8 eV [107-109]. Herein we utilized an excitation wavelength of 3.54 eV to report PL activities below the usual band gap energy. Figure 24 shows two major peaks around 560 nm (2.21 eV) and 675 nm (1.84 eV). As noted previously, these emissions can be attributed to the recombination of electrons and holes from the conduction and valence band [94]. In order to further investigate the nature of these emissions it is necessary to analyze the possible transitions occurring in the free-electron model of MgO as illustrated in Figure 25 below.

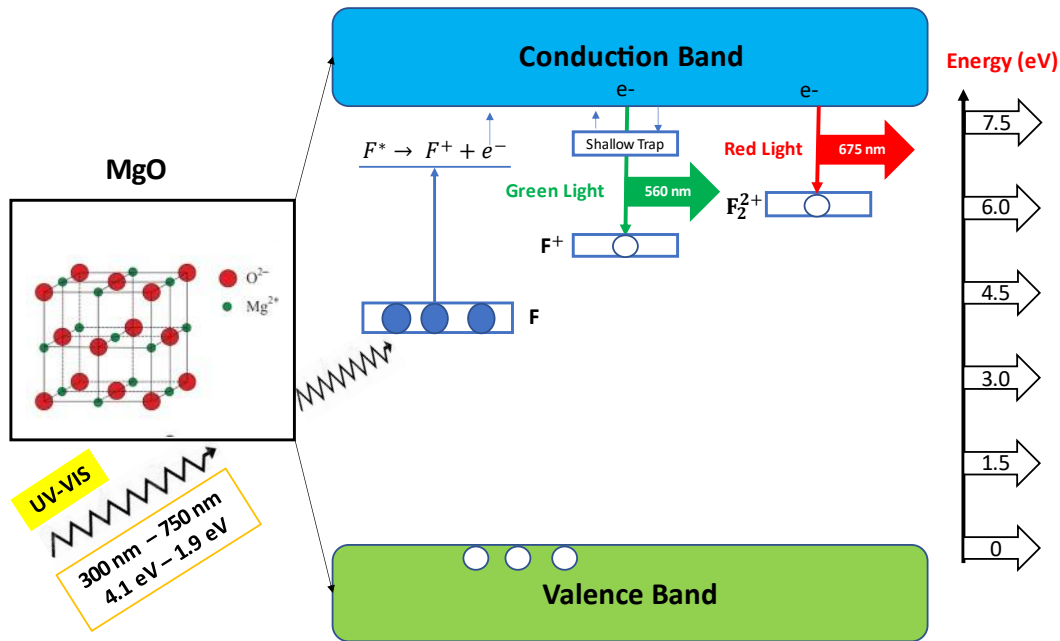


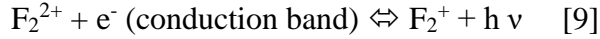
Figure 25: A free-electron model demonstrating possible electron-hole recombination. The blue-filled circles represent occupied electronic states, whereas the white ones represent vacant electronic states or holes. White circles in the valence band demonstrate cationic holes.

Utilizing UV-Visible light spectroscopy (UV-VIS), the MgO samples were illuminated with electromagnetic rays of wavelengths ranging from 300 nm corresponding to the ultraviolet (UV) spectrum up to wavelengths of 750 nm associated with the visible light (VIS) spectrum. It is worth noting that neutral oxygen vacancies denoted as F centers exist within the bandgap of MgO between the range of 3.0 – 4.5 eV [61]. As a result of UV-VIS illumination, electrons trapped in F centers undergo a photo conversion process, where the trapped electrons either get promoted to the conduction band or get stuck in shallow traps close to the conduction band. As the photoconversion process occurs, cationic oxygen vacancies (denoted with F^+ centers) and clustered cationic oxygen vacancies (denoted with F_2^{2+}) form at 5.4 and 6.0 eV, respectively.

The first photoluminescent peak at 560 nm can be associated with green field emissions in the visible region as an electron in the conduction band or a shallow trap (below the conduction band) recombines with a cationic oxygen vacancy [61].



The second photoluminescent peak at 675 nm can be associated with red field emissions in the visible region as an electron in the conduction band recombines with a dicationic oxygen-cluster vacancy [61].



When comparing the undoped MgO with the MgO:V0.7 sample in Figure 24, it can be seen that doping with V flattens the PL emission signals, which implies that the introduction of dopant-induced extrinsic defects suppressed the effect of intrinsic defects, further implying the successful incorporation of V into the MgO lattice, and affirming the XRD and EDS results. Furthermore, at both peak signals, it was revealed that the MgO:V0.7 sample displayed a reduced PL intensity when compared to the undoped MgO sample, thus signifying reduced optical activity with the insertion of the dopant. Consequently, a correlation between these PL results and the performance of the constructed supercapacitors is discussed later in Chapter 5.6. The MgO:V0.7 sample reveals the lowest values of PL peaks intensities, indicating a reduction in vacancies and a lower recombination rate of electrons and holes, thus providing more charge carriers at excited states that, in turn, increase the performance of the supercapacitor device.

In order to calculate the band gap energies of the undoped and MgO:V0.7 samples, Tauc plots were constructed by normalizing the transmittance as the samples were swept in the UV-Visible light regions. Transmittance values were converted to absorbance, and by incorporating the absorption coefficient (α), the energy ($h\nu$) in eV was plotted against $(\alpha h\nu)^2$. Figure 26 displays the Tauc plots of the undoped and MgO:V0.7 samples, where the intersection of the linear portions of the curves with the x-axis denotes the bandgap energies.

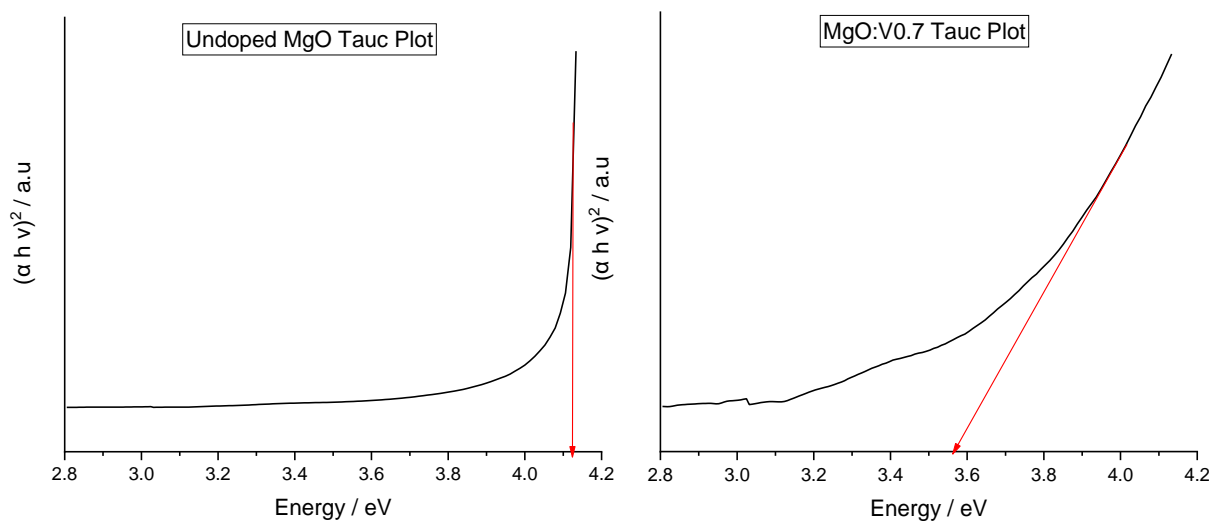


Figure 26: Tauc plots of undoped MgO (left) and MgO:V0.7 (right).

It is evident that the MgO:V0.7 sample exhibits a lower bandgap energy of approximately 3.6 eV when compared to the undoped MgO sample, which was found to have a bandgap energy of approximately 4.1 eV. Diachenko *et al.* reported bandgap energy values between 4.1 and 4.6 eV for MgO nanofilms synthesized via chemical precipitation, similar to this work's synthesis route [110]. Thus, the introduction of V dopant in the MgO structure reduced the gap between the valence and conduction bands, increasing the conductivity of the doped material, and ultimately improving the electrochemical performance of supercapacitors constructed with MgO:V0.7 electrodes as discussed further in Chapter 5.6. Figure 27 below presents a visual demonstration of the calculated bandgap energies of the undoped and MgO:V0.7 samples.

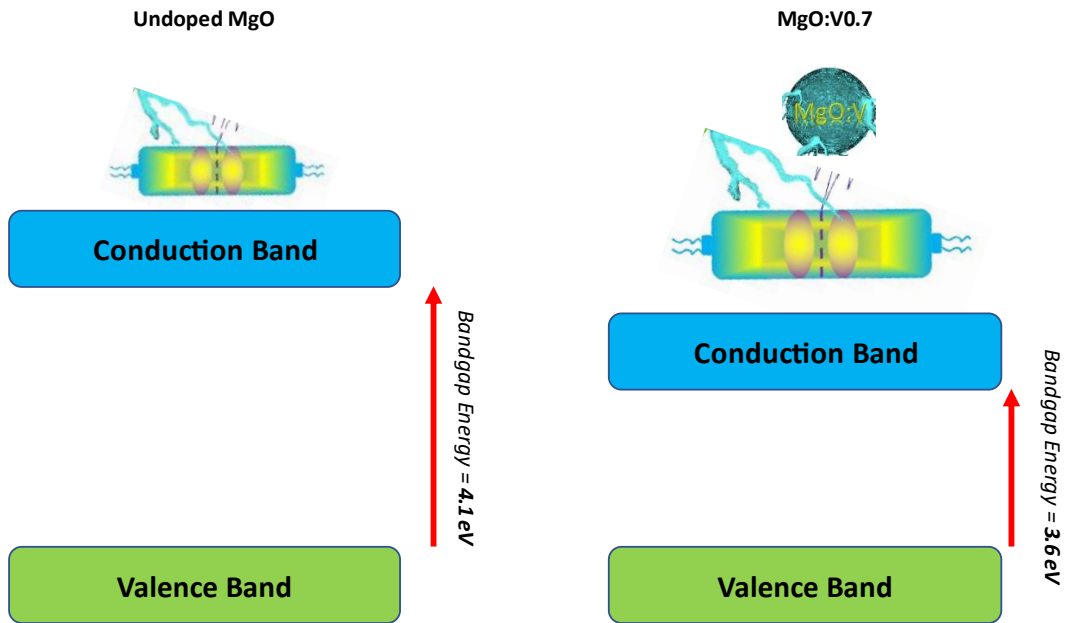


Figure 27: A visual demonstration of the bandgap energies of undoped MgO (left-side) and MgO:V0.7 (right-side).

5.6. Electrochemical Analysis

Four symmetric supercapacitors with identical undoped and V-doped MgO electrodes were designed, as presented in Figure 9, to evaluate their electrochemical performance. A concentrated 6 M KOH electrolyte solution was utilized instead of a standard 1 M solution to avoid oxygen evolution reaction (OER) associated with water electrolysis at higher voltage windows.

5.6.1. Cyclic Voltammetry (CV)

CV tests were performed on all supercapacitors to acquire information on electrochemical activity, conductivity, and the chemical/physical mechanism type. At a scan rate of 50 mV/s, the potential is swept from 0 to 1 V (voltage window) as the current response is recorded to generate cyclic voltammograms shown in Figure 28.

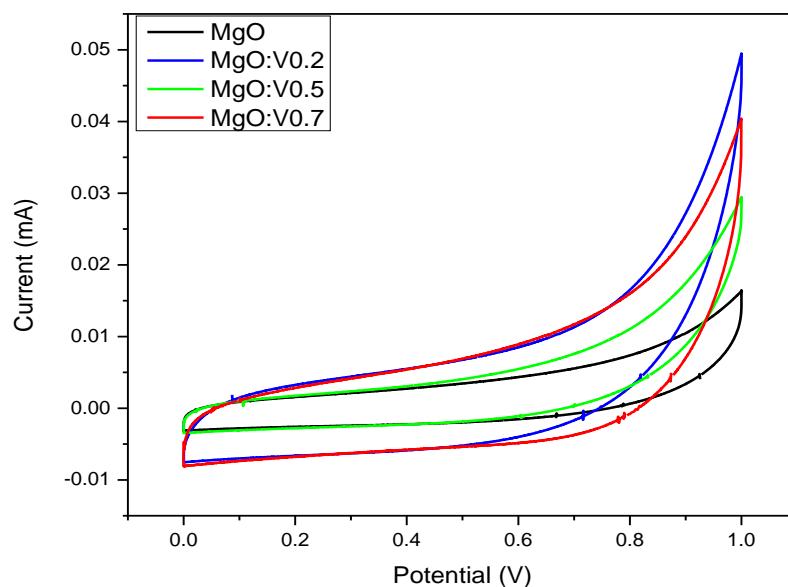


Figure 28: Cyclic voltammetry of the MgO:V_x samples carried out between 0 and 1 V at a scan rate of 50 mV/s.

The measured voltammograms for the MgO-based materials deviate from the ideal rectangular shape associated with EDLCs and the inverted pyramid shape observed in typical batteries. Instead, a quasi-rectangular shape is detected, implying pseudocapacitive behavior, where only a small fraction of the charge is due to EDLC. A major part of charge transfer and storage is attributed to fast and reversible faradaic reactions (redox reactions, intercalation, and electrosorption) occurring at the electrode surfaces, and resulting in higher energy densities and specific capacitances than for EDLCs, yet at the expense of a reduction in power density and cyclic stability [111]. The area under the voltammograms represents the amount of charge actively participating on the electrode surface, thus leading to specific capacitance (C_p) values. By employing a Poly Area function, the area of the voltammograms is computed and used in Equation 10 below [112] to obtain the C_p values. The results are summarized in Figure 29.

$$C_p = \frac{\int_{V_i}^{V_f} I dV}{2 \times m \times v \times (V_f - V_i)} \quad [10]$$

C_p : specific capacitance (F/g)

$\int_{V_i}^{V_f} I dV$: area of voltammogram computed by Origin Poly Area function

V_i : initial voltage (= 0 V)

V_f : final voltage (= 1 V)

m : mass of the sample (= 4 mg)

v : scan rate (= 50 mV/s)

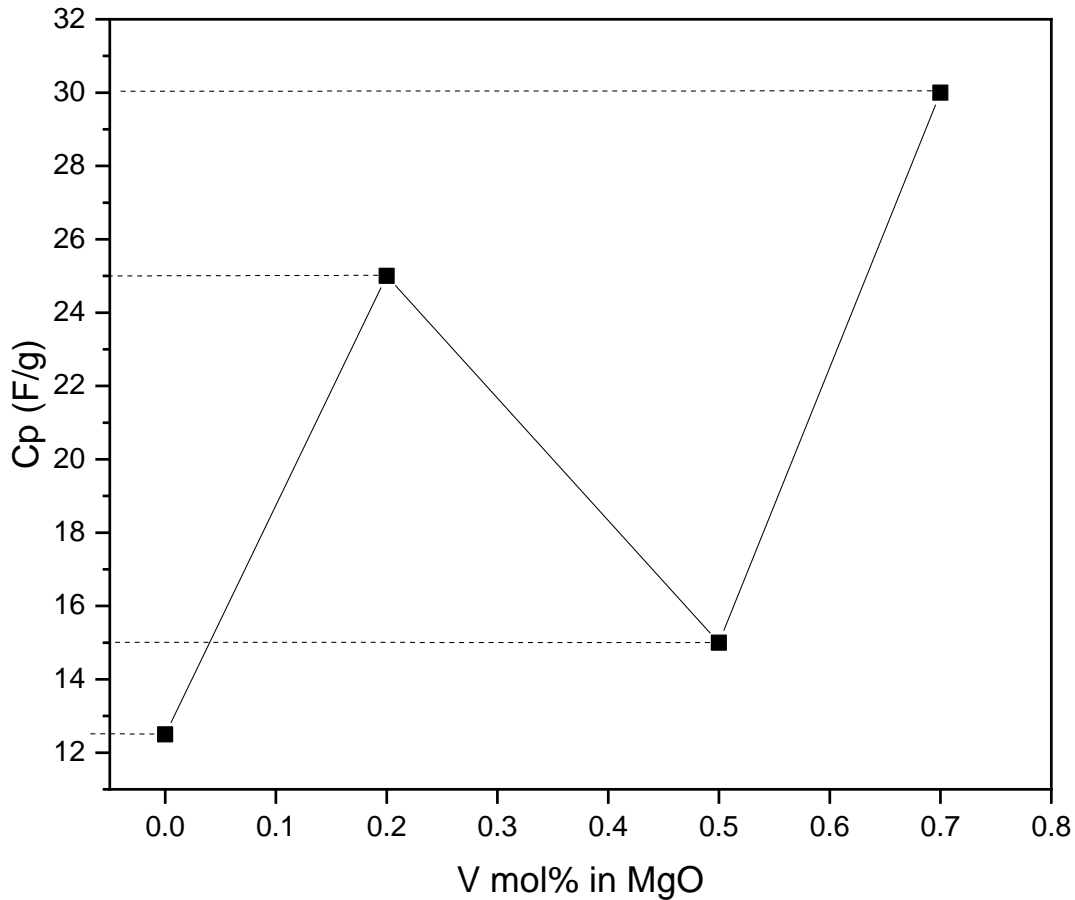


Figure 29: C_p values obtained for MgO:Vx samples from CV curves at a scan rate of 50 mV/s.

Comparing the obtained C_p values of the MgO:V0.7 sample (30 F/g) with the undoped MgO sample (12.5 F/g) shows that the V-doping enhances the electrical properties of the host material. Considering the average crystalline sizes obtained from the XRD diffractograms analysis in Figure 13, where the MgO:V0.7 sample presented the largest crystallite size (≈ 7.75 nm) as compared to the undoped sample with the smallest crystalline size (≈ 6.25 nm), it can be assumed that a greater average crystallite size implies a more significant nanolayered structure and a higher electrochemical surface area, eventually leading to electrons interacting with a greater number of active sites [113]. Additionally, the improved performance of the V-doped samples compared to the pure MgO sample can be attributed to the extrinsic defects introduced into the semi-crystalline structure of MgO, as evidenced by the PL and EPR results, where the MgO:V0.7 sample illustrated the lowest optical activity yet highest electron spin density.

Since the MgO:V0.7 sample showed the most promising electrochemical performance in the CV analysis, an additional investigation was carried out to optimize the supercapacitor's specific capacitance and energy density. Thus, a CV test was conducted for the MgO:V0.7 sample at different scan rates, as shown in Figure 30. Subsequently, the C_p values were calculated from Equation 10 and plotted as a function of the scan rates as displayed in Figure 31.

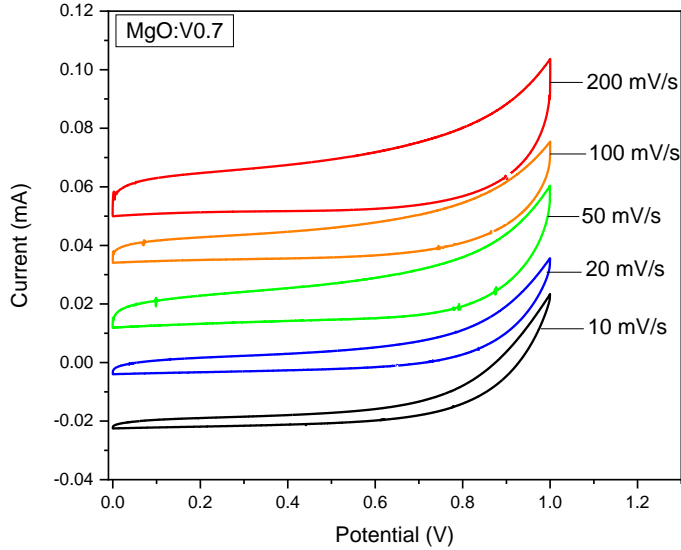


Figure 30: CV of the MgO:V0.7 sample carried out between 0 and 1 V at different scan rates.

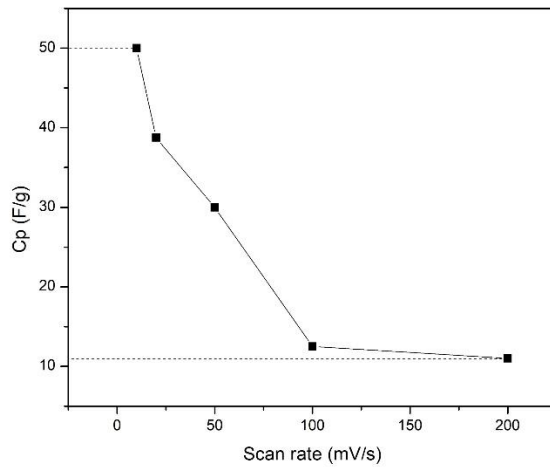


Figure 31: C_p values obtained for the MgO:V0.7 sample at different scan rates.

It is evident that as the scan rate increases, the C_p values drop, and ultimately the energy density decreases because the ions have a narrower time range to react, thus a smaller surface response. At scan rates of 100 and 200 mV/s, the ions/electrons have less residence time, so redox reactions involved in diffusion-dominated ionic transport at electrode/electrolyte interfaces are restricted. Alternatively, reducing the scan rate enables more accumulated charge to diffuse through the material smoothly; thus, higher capacitance values are obtained [114]. Since higher C_p values (50 F/g at 10 mV/s) were obtained at lower scan rates for MgO:V0.7, this reflects the effective synergy between the supercapacitor components and good stability before degradation. Karthikeyan *et al.* reported a specific capacitance of approximately 50 F/g for asymmetric MgO-MWCNT electrode supercapacitors at a scan rate of 50 mV/s, additionally concluding the inverse relationship between the scan rate and specific capacitance and attributing this to surface adsorption processes and reduction of ion mobility [115]. The C_p value of 50 F/g at a 10 mV/s scan rate is an important finding since no booster material like carbon was used for this symmetric supercapacitor design. The enhanced values can be attributed to the highly defective nature of the MgO:V0.7 sample, as shown in the previous EPR and PL Chapters 5.4 and 5.5.

Since the MgO:V0.7 sample displayed the best electrical properties as a symmetric supercapacitor, further analysis was carried out by designing an asymmetric supercapacitor with one electrode fabricated from MgO:V0.7, and the counter electrode constructed from carbon black (CB). Figure 32 demonstrates the C_p values (obtained from the CV curves and Equation 10) of the mentioned asymmetric supercapacitor as a function of the scan rate, where symmetric C_p values were plotted on the same scale for comparison purposes. The asymmetric supercapacitor device shows a tremendous increase of the C_p values at all scan rates, when compared against symmetric supercapacitors, reaching a peak value of 1200 F/g at 20 mV/s. The significant increase in the C_p values can be attributed to the improved synergy of the asymmetric electrode materials. In addition to that, CB is well known for its high surface-to-volume ratio [116, 117]. While the main focus of this thesis was dedicated to symmetric supercapacitors displaying promising performance complementary to previous studies [115], such analysis of asymmetric supercapacitors increases the applicability potential of MgO-based electrode materials.

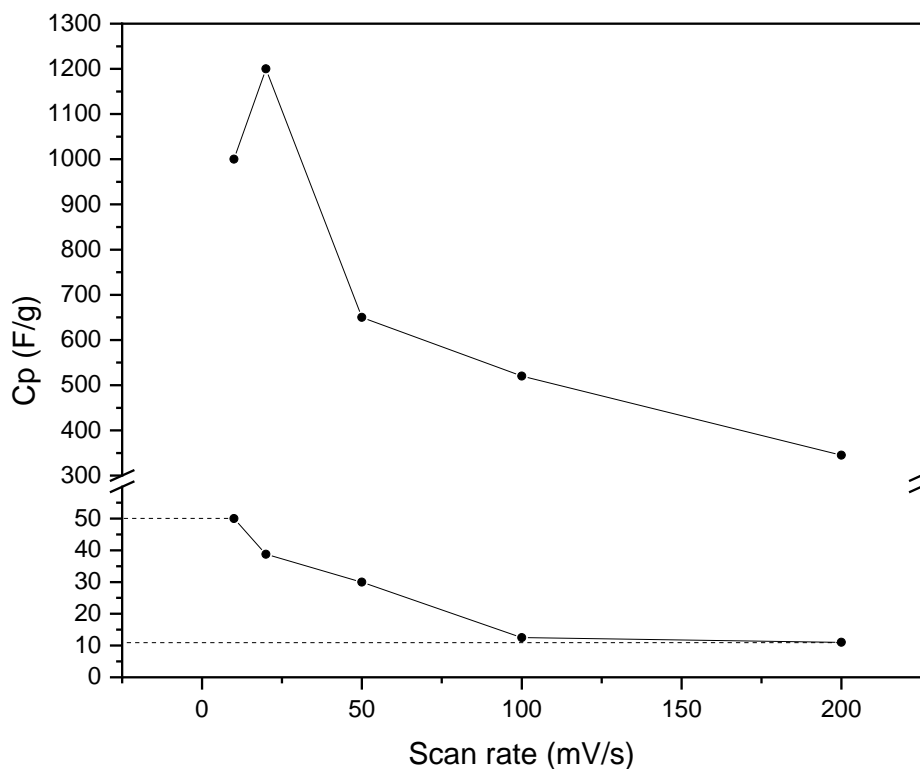


Figure 32: C_p values plotted as a function of the scan rate for the MgO:V0.7 sample in symmetric (below) and CB-asymmetric (above) supercapacitor devices.

5.6.2. Electrochemical Impedance Spectroscopy (EIS)

The impedance of the MgO:V_x supercapacitor devices were assessed with EIS by applying an AC voltage and recording the real impedance values against the negative imaginary impedance on a Nyquist Plot as shown in Figure 33. Although this would provide further insight into the kinetic properties of the electrodes, it is expected that metal oxide electrodes (as in our case MgO) generally display resistive instead of conductive behavior before eventual degradation [8].

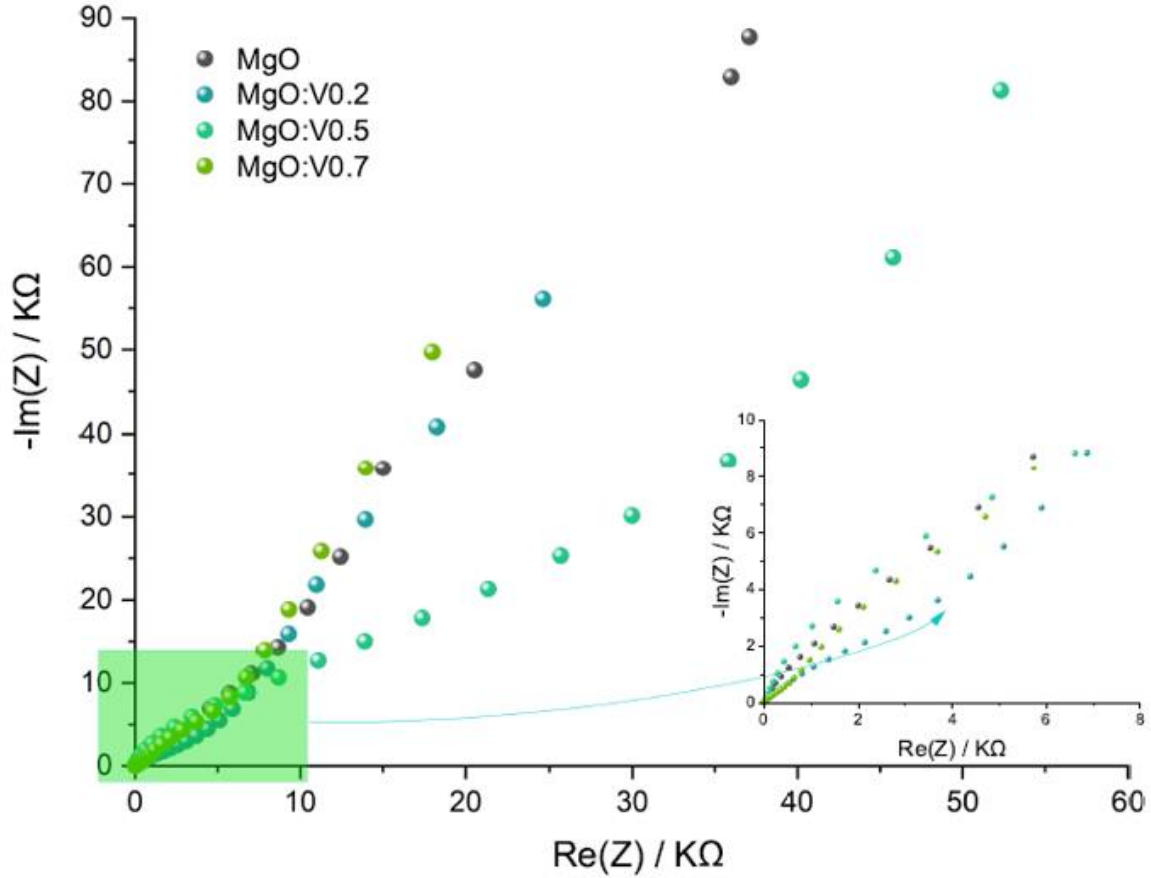


Figure 33: Nyquist Plot of the MgO:V_x supercapacitor devices. The inset highlights the high-frequency zone.

The Nyquist Plot curves can be split into three different segments of interest: the x-intercept in the high-frequency zone, which represents the sum of the electrolyte's ionic resistance, the electrode's intrinsic resistance, and the interface resistance in what is referred to as the Equivalent Series Resistance (R_s); the diameter curvature in the high-frequency zone signifies the Charge Transfer Resistance (R_{ct}); and the linear slope in the low-frequency zone correlates to the Diffusion Resistance of the hydroxyl ions into the electrodes [118]. Utilizing the Z-Fit tool in the EC-Lab® program, equivalent circuit fits were produced for the undoped MgO and MgO:V0.7 samples, with a particular focus on the high-frequency zone (0 – 15 Ω), to compute the R_s values. Figure 34 displays the Z-Fits in addition to the equivalent circuit scheme and

computed R_s values. Table 4 summarizes the values of the electronic parameters comprising the equivalent circuits.

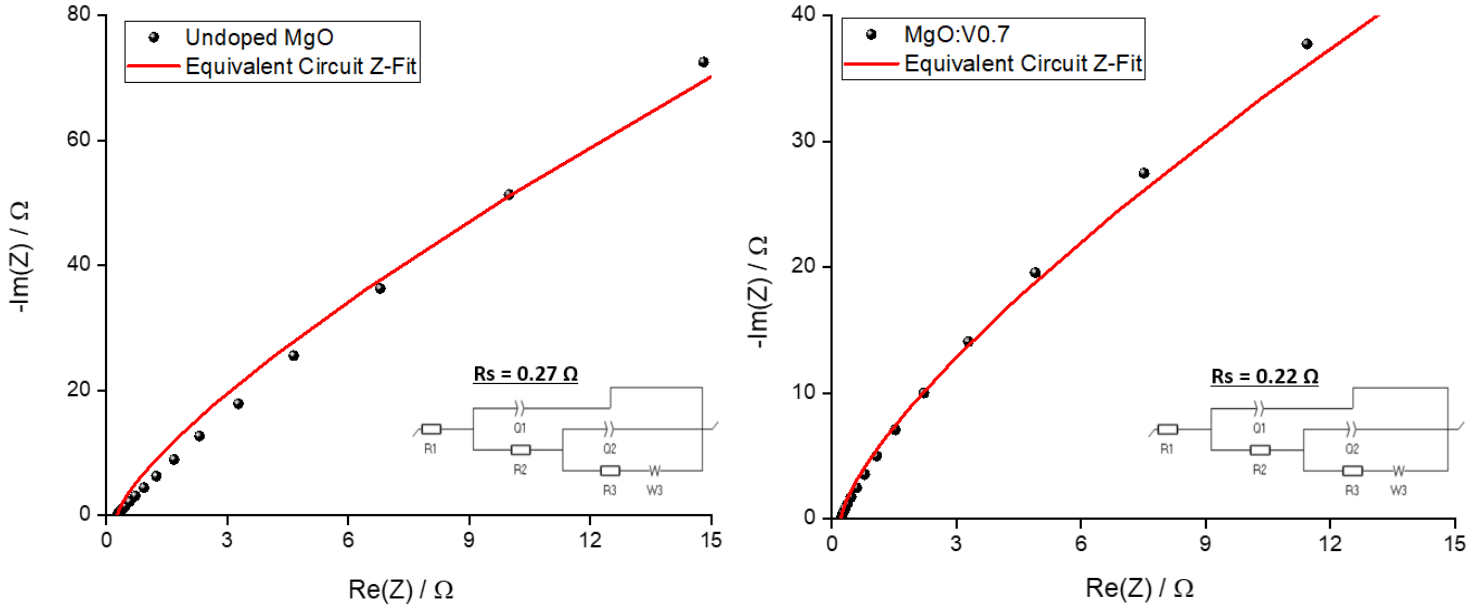


Figure 34: Z-Fits & equivalent circuits of Nyquist Plots in the high-frequency zone of undoped MgO (left-side) and MgO:V0.7 (right-side)

Table 4: A summary of the values of the electronic parameters comprising the equivalent circuits.

	$R_1 (\Omega)$	$R_2 (\Omega)$	$R_3 (\Omega)$	$Q_1 (F/s)$	$Q_2 (F/s)$	$W_3 (\Omega.s^{-1/2})$	$R_s (\Omega)$
MgO	0.25	9.53×10^{-3}	3.03×10^{-9}	≈ 0	11.35×10^{-6}	15000	0.27
MgO:V0.7	0.22	19.71	4.35	6.38×10^{-6}	≈ 0	5000	0.22

The R_s value obtained for the MgO:V0.7 and undoped MgO-based supercapacitors were 0.22 and 0.27 Ω , respectively. The R_{ct} value of both supercapacitors is negligible, indicating negligible charge transfer or low faradaic resistance since the curvatures in the high-frequency zone are not evident. The diffusion resistances of both supercapacitors are similar since the slopes of both linear regions are almost identical. Consequently, it can be concluded that the sample with the highest doping concentration has the lowest equivalent series resistance, thus overall impedance, and simultaneously shows the best capacitance and energy density. This was affirmed by the PL analysis where MgO:V0.7 displayed the least optical activity as V-induced defects trapped electrons at high energy bands near the conduction band instead of allowing them to recombine with lower energy state holes. Thus, higher conductance, and ultimately lower impedance, was anticipated for the MgO:V0.7 sample.

5.6.3. Galvanostatic Charge-Discharge with Potential Limitation (GCPL)

A GCPL assessment was utilized to compute the discharge time of the MgO:V_x samples with a voltage window from 0 to +1 V at a specific current of 0.6 A/g (discharge current of 2.40 mA and a standard 4 mg sample mass). Subsequently, the energy and power densities of the constructed symmetric supercapacitors were calculated based on Equations 11 and 12 [112], and the results are summarized in a Ragone Plot in Figure 35.

$$\text{Energy Density } \left(\frac{Wh}{kg} \right) = \frac{1}{2} \frac{Cp (V_f - V_i)^2}{3.6} \quad [11]$$

$$\text{Power Density } \left(\frac{W}{kg} \right) = \frac{\text{Energy Density} \times 3600}{\text{Discharge Time}} \quad [12]$$

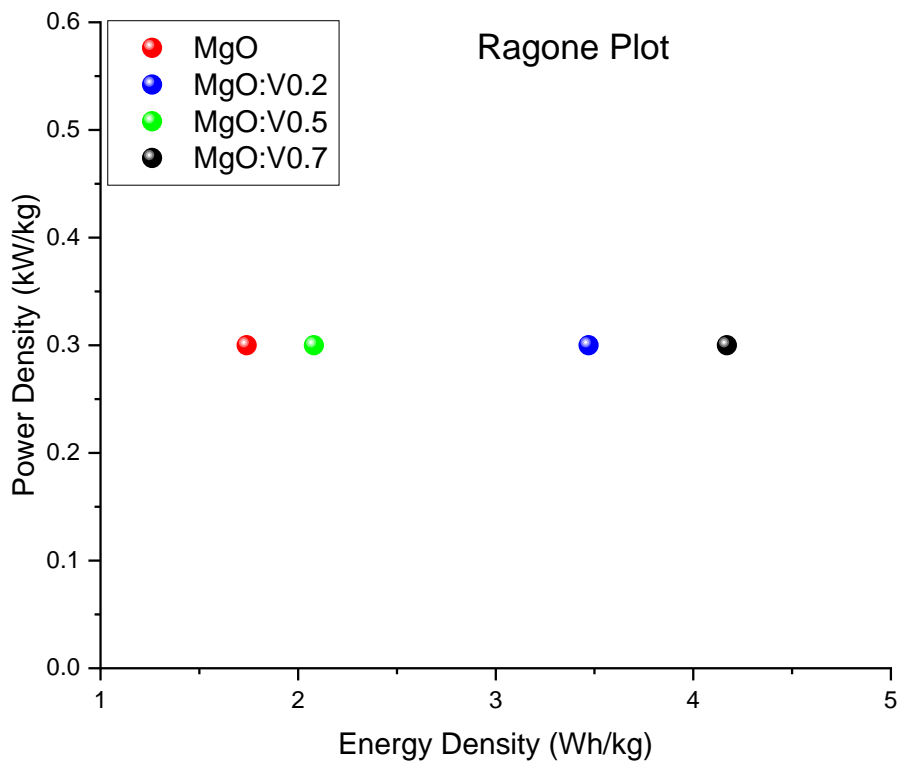


Figure 35: A Ragone Plot showing the energy and power densities for the MgO:V_x samples.

The MgO:V0.7 sample has the highest energy density of 4.17 Wh/kg. In contrast, the undoped sample has the lowest energy density of 1.74 Wh/kg, implying that a higher V-dopant concentration leads to greater capacitance values and energy densities, ultimately signifying enhanced electrochemical performance.

Furthermore, the reversibility of the fabricated pure MgO and MgO:V0.7 electrodes was investigated through GCPL tests at a 0.6 A/g current density and with a voltage window of 1 V. Figure 36 conveys the electrochemical reversibility and stability of the MgO electrodes in their undoped and doped states, where the cell potential displayed a linear and symmetrical time dependence during the measurement cycles. In addition, the fact that the charge and discharge curves overlap each other, as seen in Figure 36, confirms the reversibility of the fabricated electrodes [115].

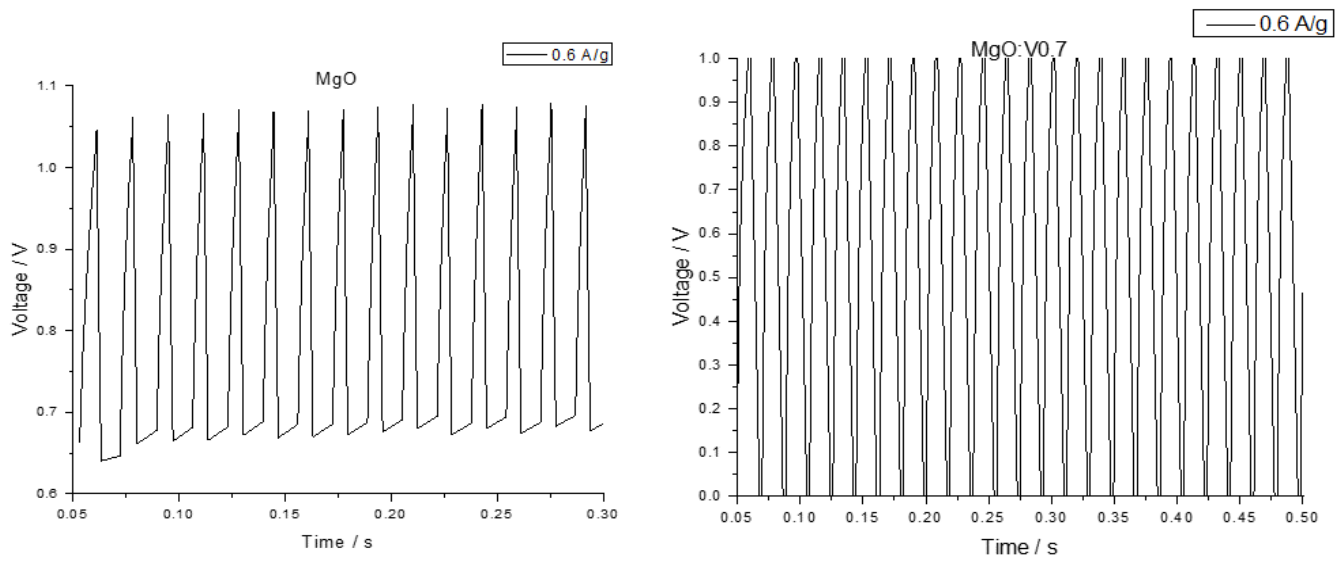
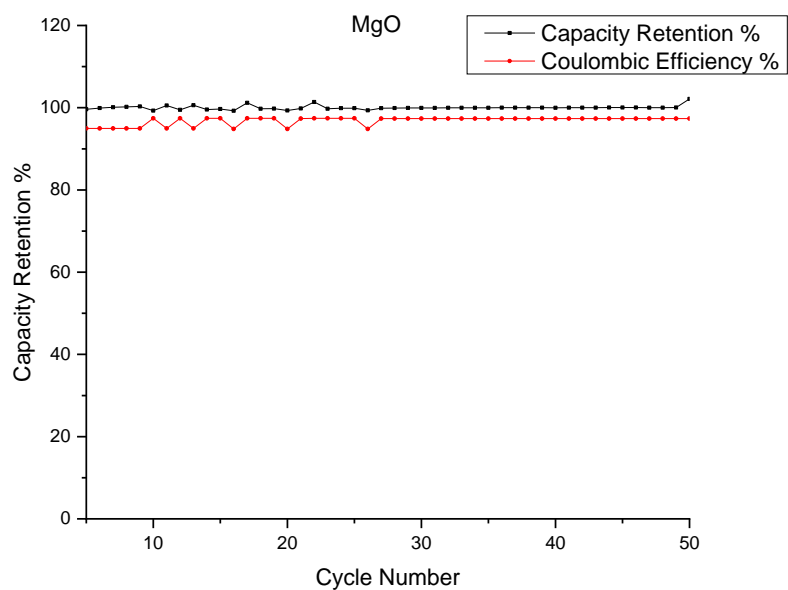


Figure 36: GCPL electrochemical reversibility assessment for undoped MgO (left-side) and MgO:V0.7 (right-side).

The long-term electrochemical performance was investigated by examining the capacity retention and coulombic efficiency over several number of cycles. Figure 37 confirms the excellent cyclic stability of the undoped and V-doped MgO-based electrodes, where both cases displayed capacity retention and Coulombic efficiencies above 90% after 50 cycles.

(a)



(b)

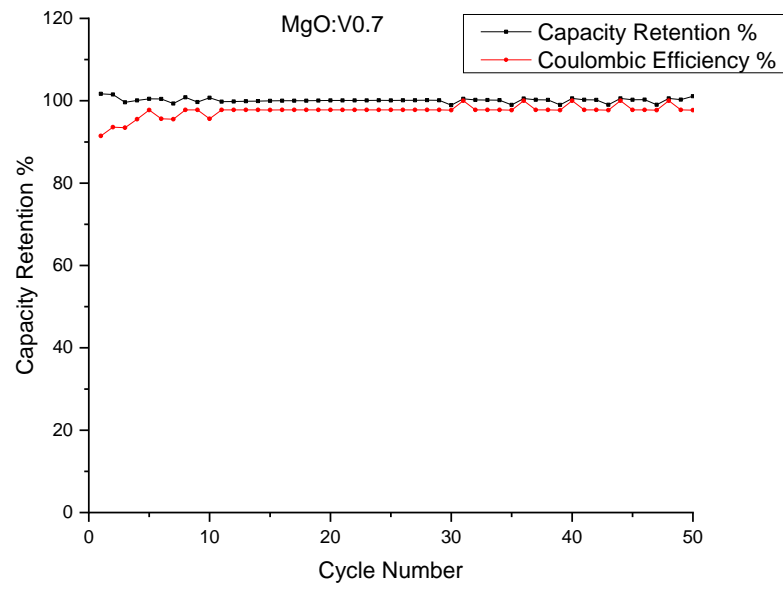


Figure 37: GCPL cyclic stability assessment for (a) undoped MgO, and (b) MgO:V0.7 through a measure of capacity retention and coulombic efficiency.

6. Conclusions

This thesis provides insight into the capacitive behavior of MgO, an abundant and sustainable material, highlighting the potential to utilize this non-carbon material as electrodes in the design of symmetric supercapacitor devices, which display outstanding electrochemical performances. It is worth emphasizing the fact that the purpose of this work was not to optimize the electrical performance of the constructed supercapacitors but rather to shed some light on the unique properties of MgO that make it an ideal candidate material in energy storage applications. Furthermore, in the scope of this thesis, the other aim is to stress the significance of V^{4+} ions as paramagnetic probing agents that reveal much of the electronic and optical properties of MgO, that otherwise would not be possible due to the diamagnetism of MgO, as well as to underline the prominence of doping in introducing extrinsic defects into a material, and ultimately improving the electrochemical performance of energy storage devices.

The MgO:V_x samples were synthesized through chemical precipitation, owing to its simplicity and low cost, where undoped, 0.2, 0.5, and 0.7 mol% V-doped MgO samples were prepared (MgO, MgO:V0.2, MgO:V0.5, and MgO:V0.7). Characterization techniques were utilized to investigate the structural, electronic, and optical properties of the MgO:V_x samples, and to explore the electrochemical performance of the constructed supercapacitors with the MgO:V_x samples as electrodes. XRD revealed information about the crystalline structure of the MgO:V_x samples, where average crystalline sizes were calculated by employing Scherrer's Equation and W-H Plots. A Rietveld refinement was included to investigate the effect of V-doping on the crystal structure of MgO. STEM images provided insight into the nanostructure and morphology of the synthesized samples, where average particle sizes were calculated and compared to average crystalline sizes. A Raman analysis was conducted to study the chemical structure and vibrational modes of the samples, where it was reinforced with EDS analysis to confirm the success of doping and the presence of the V^{4+} ions. EPR analysis revealed the intrinsic and extrinsic defects in the MgO:V_x samples, where an Aniso-Spin fit was simulated to obtain electron spin densities. The optical properties of the samples were investigated by means of PL spectroscopy, emphasizing the free-electron core-shell model, analyzing the intrinsic defects in the UV-VIS range, and calculating the band-gap energies from Tauc plots. Eventually, EC

measurements (CV, EIS, and GCPL) were employed to test the electrochemical performance of the constructed supercapacitors. Consequently, specific capacitances and energy densities were calculated, while voltammograms, Nyquist plots, and Ragone plots were constructed. Correlations between the several characterization techniques were established, and the results proved to complement one another.

While the energy storage applications of MgO are still in the early stages of development, ongoing research suggests that its capabilities in this area could be expanded in the future. Even though the electrical properties of MgO are limited due to the large band gap (up to 7.8 eV), doping the material with paramagnetic V-ions enhanced its electrical properties, making it possible to use it as an electrode material in symmetric supercapacitor devices with no additional booster material like carbon. The cyclic voltammetry suggested that MgO:V0.7 exhibited excellent capacitance behavior between 0 and 1 V at low scan rates, delivering a maximum specific capacitance of 50 F/g and an energy density of 4.14 Wh/kg at 10 mV/s scan. The enhanced performance of such symmetric supercapacitors is mainly due to the electro-catalytic activity of MgO and the induced V-based defects. For comparison purposes, one asymmetric supercapacitor device was constructed with the MgO:V0.7 sample as one electrode and CB as a counter electrode, where a tremendous increase in C_p values was achieved at all scan rates, reaching a peak value of 1200 F/g at 20 mV/s. The low cost and environmentally-friendly nature of MgO with high specific capacitance and energy density empower the possibility of using them in practical energy-storage applications, as we have successfully proven in our latest publication in the Journal of Alloys and Compounds, titled “Vanadium-Doped Magnesium Oxide Nanoparticles as Electrodes in Supercapacitor Devices” [119].

This thesis provides encouraging results that yield the way for future work and publications we plan to pursue. The effect of ball-milling on the structural properties of the samples, and eventually the electrochemical performance of the supercapacitors, can be investigated. Furthermore, the selection of alternative electrolyte materials provides an interesting perspective for research as different electrolytes correspond to different voltage windows, and thus influence the electrochemical performances. Moreover, this work can be extended into optimizing the performance of asymmetric supercapacitors with the MgO:V_x samples and other unique materials comprising the counter-electrode.

7. References:

- [1] J. L. Holechek *et al.*, "A global assessment: can renewable energy replace fossil fuels by 2050?," *Sustainability*, vol. 14, no. 8, p. 4792, 2022.
- [2] S. Manzoor *et al.*, "Flowery In_2MnSe_4 novel electrocatalyst developed via anion exchange strategy for efficient water splitting," *Nanomaterials*, vol. 12, p. 2209, 2022.
- [3] M. Hassan *et al.*, "Structural parameters, energy states and magnetic properties of the novel Se-doped NiFe_2O_4 ferrites as highly efficient electrocatalysts for HER," *Ceramics International*, vol. 48, pp. 24866-24876, 2022.
- [4] E. Erdem, "Why P2X must be the part of the energy solution?," *Environmental Progress & Sustainable Energy*, vol. 40, p.13545, 2021.
- [5] J. Zhao *et al.*, "Review on supercapacitors: Technologies and performance evaluation," *Journal of energy chemistry*, vol. 59, pp. 276-291, 2021.
- [6] P. Sharma *et al.*, "Current technology of supercapacitors: A review," *Journal of Electronic Materials*, vol. 49, pp. 3520-3532, 2020.
- [7] J. Yan *et al.*, "Rational design of nanostructured electrode materials toward multifunctional supercapacitors," *Advanced Functional Materials*, vol. 30, p. 1902564, 2020.
- [8] A. U. Ammar *et al.*, "ZnO and MXenes as electrode materials for supercapacitor devices," *Beilstein Journal of Nanotechnology*, vol. 12, pp. 49-57, 2021.
- [9] Y. M. Volfkovich, "Supercapacitors: problems and prospects of development," *Russian Chemical Reviews*, pp. 1-19, 2022.
- [10] S. Kasap *et al.*, "Superbat: battery-like supercapacitor utilized by graphene foam and zinc oxide (ZnO) electrodes induced by structural defects," *Nanoscale Advances*, vol. 1, pp. 2586-2597, 2019.
- [11] R. Genc *et al.*, "High-capacitance hybrid supercapacitor based on multi-colored fluorescent carbon-dots," *Scientific reports*, vol. 7, p. 11222, 2017.
- [12] S. Chen *et al.*, "Graphene oxide– MnO_2 nanocomposites for supercapacitors," *ACS nano*, vol. 4, pp. 2822-2830, 2010.
- [13] S. K. Meher *et al.*, "Ultralayered Co_3O_4 for high-performance supercapacitor applications," *The Journal of Physical Chemistry C*, vol. 115, pp. 15646-15654, 2011.
- [14] M. Zdorovets *et al.*, "Phase transformations in FeCo – $\text{Fe}_2\text{CoO}_4/\text{Co}_3\text{O}_4$ -spinel nanostructures as a result of thermal annealing and their practical application," *Journal of Materials Science: Materials in Electronics*, vol. 32, pp. 16694-16705, 2021.

- [15] A. Trukhanov *et al.*, "Evolution of structure and physical properties in Al-substituted Ba-hexaferrites," *Chinese Physics B*, vol. 25, p. 016102, 2015.
- [16] M. Abdel Maksoud *et al.*, "Advanced materials and technologies for supercapacitors used in energy conversion and storage: a review," *Environmental Chemistry Letters*, vol. 19, pp. 375-439, 2021.
- [17] B. Xu *et al.*, "Highly mesoporous and high surface area carbon: A high capacitance electrode material for EDLCs with various electrolytes," *Electrochemistry Communications*, vol. 10, pp. 795-797, 2008.
- [18] S. A. Khan *et al.*, "Synthesis and Characterization of Composites with Y-Hexaferrites for Electromagnetic Interference Shielding Applications," *Magnetochemistry*, vol. 8, p. 186, 2022.
- [19] G. Mineo *et al.*, "Advances in WO₃-Based Supercapacitors: State-of-the-Art Research and Future Perspectives," *Nanomaterials*, vol. 13, p. 1418, 2023.
- [20] Z. Ning *et al.*, "Quantum-dot-in-perovskite solids," *Nature*, vol. 523, pp. 324-328, 2015.
- [21] I. Villa *et al.*, "Size-dependent luminescence in HfO₂ nanocrystals: Toward white emission from intrinsic surface defects," *Chemistry of Materials*, vol. 28, pp. 3245-3253, 2016.
- [22] M. Altmeyer *et al.*, "Magnetism, spin texture, and in-gap states: atomic specialization at the surface of oxygen-deficient SrTiO₃," *Physical review letters*, vol. 116, p. 157203, 2016.
- [23] J. Nowotny *et al.*, "Defect chemistry and defect engineering of TiO₂-based semiconductors for solar energy conversion," *Chemical Society Reviews*, vol. 44, pp. 8424-8442, 2015.
- [24] L. Kong *et al.*, "Defect-induced yellow color in Nb-doped TiO₂ and its impact on visible-light photocatalysis," *The Journal of Physical Chemistry C*, vol. 119, pp. 16623-16632, 2015.
- [25] B. Zheng *et al.*, "Rare-earth doping in nanostructured inorganic materials," *Chemical Reviews*, vol. 122, pp. 5519-5603, 2022.
- [26] M. Sterrer *et al.*, "Energy transfer on the MgO surface, monitored by UV- induced H₂ chemisorption," *Journal of the American Chemical Society*, vol. 125, pp. 195-199, 2003.
- [27] X.-Y. Yu *et al.*, "Porous hierarchically micro-/nanostructured MgO: morphology control and their excellent performance in As (III) and As (V) removal," *The Journal of Physical Chemistry C*, vol. 115, pp. 22242-22250, 2011.
- [28] A. J. Haes *et al.*, "A nanoscale optical biosensor: the long range distance dependence of the localized surface plasmon resonance of noble metal nanoparticles," *The Journal of Physical Chemistry B*, vol. 108, pp. 109-116, 2004.
- [29] S.-W. Bian *et al.*, "A template-free, thermal decomposition method to synthesize mesoporous MgO with a nanocrystalline framework and its application in carbon dioxide adsorption," *Journal of Materials Chemistry*, vol. 20, pp. 8705-8710, 2010.
- [30] J. González *et al.*, "Electron confinement induced by diluted hydrogen-like ad-atoms in graphene ribbons," *Physical Chemistry Chemical Physics*, vol. 17, pp. 24707-24715, 2015.

- [31] U. K. Gaur *et al.*, "Fe-induced morphological transformation of 1-D CuO nanochains to porous nanofibers with enhanced optical, magnetic and ferroelectric properties," *Journal of Materials Chemistry C*, vol. 3, pp. 4297-4307, 2015.
- [32] C. Park *et al.*, "Geometrical separation of defect states in ZnO nanorods and their morphology-dependent correlation between photoluminescence and photoconductivity," *The Journal of Physical Chemistry C*, vol. 119, pp. 16984-16990, 2015.
- [33] E. Erdem *et al.*, "Microwave power, temperature, atmospheric and light dependence of intrinsic defects in ZnO nanoparticles: A study of electron paramagnetic resonance (EPR) spectroscopy," *Journal of Alloys and Compounds*, vol. 605, pp. 34-44, 2014.
- [34] H. Kaftelen *et al.*, "EPR and photoluminescence spectroscopy studies on the defect structure of ZnO nanocrystals," *Physical Review B*, vol. 86, p. 014113, 2012.
- [35] J. Li *et al.*, "Nanoscale clarification of the electronic structure and optical properties of TiO₂ nanowire with an impurity phase upon sodium intercalation," *The Journal of Physical Chemistry C*, vol. 119, pp. 17848-17856, 2015.
- [36] A. Kar *et al.*, "Surface defect-related luminescence properties of SnO₂ nanorods and nanoparticles," *The Journal of Physical Chemistry C*, vol. 115, pp. 118-124, 2011.
- [37] S. Saha *et al.*, "Bane to boon: tailored defect induced bright red luminescence from cuprous iodide nanophosphors for on-demand rare-earth-free energy-saving lighting applications," *Journal of Materials Chemistry C*, vol. 3, pp. 6786-6795, 2015.
- [38] S. Ikeda *et al.*, "Temperature and Excitation Energy Dependence of the Photoionization of the F₂ Center in α -Al₂O₃," *The Journal of Physical Chemistry C*, vol. 118, pp. 4346-4353, 2014.
- [39] P. V. Pikhitsa *et al.*, "Two-band luminescence from an intrinsic defect in spherical and terraced MgO nanoparticles," *Applied Physics Letters*, vol. 106, p. 183106, 2015.
- [40] J. Hornak *et al.*, "Synthesis, properties, and selected technical applications of magnesium oxide nanoparticles: a review," *International Journal of Molecular Sciences*, vol. 22, p. 12752, 2021.
- [41] P. Hu *et al.*, "Vanadium Oxide: Phase Diagrams, Structures, Synthesis, and Applications," *Chemical Reviews*, 2023.
- [42] H. R. Patil *et al.*, "Vanadium-doped magnesium oxide nanoparticles formation in presence of ionic liquids and their use in photocatalytic degradation of methylene blue," *Acta Metallurgica Sinica (English Letters)*, vol. 29, pp. 253-264, 2016.
- [43] M. Winter *et al.*, "What Are Batteries, Fuel Cells, and Supercapacitors?," *Chemical Reviews*, vol. 105, pp. 1021-1021, 2005.
- [44] P. E. Lokhande *et al.*, U. S. Chavan, and A. Pandey, "Materials and fabrication methods for electrochemical supercapacitors: overview," *Electrochemical Energy Reviews*, vol. 3, pp. 155-186, 2020.

- [45] J. Chmiola *et al.*, "Anomalous increase in carbon capacitance at pore sizes less than 1 nanometer," *science*, vol. 313, pp. 1760-1763, 2006.
- [46] A. C. Forse *et al.*, "New perspectives on the charging mechanisms of supercapacitors," *Journal of the American Chemical Society*, vol. 138, pp. 5731-5744, 2016.
- [47] J. W. Lee *et al.*, "Nanosheets based mesoporous NiO microspherical structures via facile and template-free method for high performance supercapacitors," *Electrochimica Acta*, vol. 56, pp. 4849-4857, 2011.
- [48] Z. Xing *et al.*, "Ni₃S₂ coated ZnO array for high-performance supercapacitors," *Journal of Power Sources*, vol. 245, pp. 463-467, 2014.
- [49] S. Najib *et al.*, "Current progress achieved in novel materials for supercapacitor electrodes: mini review," *Nanoscale Advances*, vol. 1, pp. 2817-2827, 2019.
- [50] P. Forouzandeh *et al.*, "Electrode materials for supercapacitors: a review of recent advances," *Catalysts*, vol. 10, p. 969, 2020.
- [51] J. Ding *et al.*, "Peanut shell hybrid sodium ion capacitor with extreme energy–power rivals lithium ion capacitors," *Energy & Environmental Science*, vol. 8, pp. 941-955, 2015.
- [52] H. A. Andreas *et al.*, "Self-discharge in electrochemical capacitors: a perspective article," *Journal of The Electrochemical Society*, vol. 162, p. A5047, 2015.
- [53] L. Xie *et al.*, "Hierarchical porous carbon microtubes derived from willow catkins for supercapacitor applications," *Journal of Materials Chemistry A*, vol. 4, pp. 1637-1646, 2016.
- [54] B. K. Kim *et al.*, "Electrochemical supercapacitors for energy storage and conversion," *Handbook of clean energy systems*, pp. 1-25, 2015.
- [55] L.-F. Chen *et al.*, "Synthesis of nitrogen-doped porous carbon nanofibers as an efficient electrode material for supercapacitors," *ACS nano*, vol. 6, pp. 7092-7102, 2012.
- [56] B. E. Conway *et al.*, "Transition from “supercapacitor” to “battery” behavior in electrochemical energy storage," *Journal of the Electrochemical Society*, vol. 138, p. 1539, 1991.
- [57] M. Buldu-Akturk *et al.*, "ZnO and reduced graphene oxide electrodes for all-in-one supercapacitor devices," *Nanoscale*, vol. 14, pp. 3269-3278, 2022.
- [58] S. Najib *et al.*, "Tailoring morphology to control defect structures in ZnO electrodes for high-performance supercapacitor devices," *Nanoscale*, vol. 12, pp. 16162-16172, 2020.
- [59] Y. Zhang *et al.*, "Effects of microstructure and electrochemical properties of Ti/IrO₂–SnO₂–Ta₂O₅ as anodes on binder-free asymmetric supercapacitors with Ti/RuO₂–NiO as cathodes," *Ceramics International*, vol. 46, pp. 17640-17650, 2020.
- [60] J. Gangwar *et al.*, "Prospects of Emerging Engineered Oxide Nanomaterials and their Applications," *Defence Science Journal*, vol. 66, 2016.

- [61] N. Pathak *et al.*, "Defects induced changes in the electronic structures of MgO and their correlation with the optical properties: a special case of electron–hole recombination from the conduction band," *RSC advances*, vol. 6, pp. 96398-96415, 2016.
- [62] N. Pathak *et al.*, "Defect induced ferromagnetism in MgO and its exceptional enhancement upon thermal annealing: a case of transformation of various defect states," *Physical Chemistry Chemical Physics*, vol. 19, pp. 11975-11989, 2017.
- [63] N. Pathak *et al.*, "Defect and dopant mediated optical properties in LiNbO₃ and Eu³⁺: LiNbO₃," in *Proceedings of the seventh DAE-BRNS interdisciplinary symposium on materials chemistry*, 2018.
- [64] A. Kozlovskiy *et al.*, "Effect of doping of Ce^{4+/3+} on optical, strength and shielding properties of TeO_{2-0.25} MoO_{0.25} Bi₂O_{3-x}CeO₂ glasses," *Materials Chemistry and Physics*, vol. 263, p. 124444, 2021.
- [65] T. Montini *et al.*, "Fundamentals and catalytic applications of CeO₂-based materials," *Chemical reviews*, vol. 116, pp. 5987-6041, 2016.
- [66] M. L. Kantam *et al.*, "Transfer hydrogenation of carbonyl compounds catalyzed by ruthenium nanoparticles stabilized on nanocrystalline magnesium oxide by ionic liquids," *Advanced Synthesis & Catalysis*, vol. 350, pp. 2231-2235, 2008.
- [67] K. Layek *et al.*, "Nanocrystalline magnesium oxide stabilized gold nanoparticles: an advanced nanotechnology based recyclable heterogeneous catalyst platform for the one-pot synthesis of propargylamines," *Green Chemistry*, vol. 13, pp. 2878-2887, 2011.
- [68] J. Wang *et al.*, "One-pot synthesis of water-soluble superparamagnetic iron oxide nanoparticles and their MRI contrast effects in the mouse brains," *Materials science & engineering. C, Materials for biological applications*, vol. 48, pp. 416-23, 2015.
- [69] R. Gokarakonda *et al.*, "EPR AND DSC STUDIES ON MgO–R₂O–B₂O₃–V₂O₅ ALKALI GLASSES," *Modern Physics Letters B*, vol. 22, 2011.
- [70] J. L. Boldú *et al.*, "Spectroscopic Studies of Sol–Gel Li/MgO Catalysts," *Langmuir*, vol. 15, pp. 32-35, 1999.
- [71] J. Krzystek *et al.*, "High-frequency and -field electron paramagnetic resonance of vanadium (IV, III, and II) complexes," *Coordination Chemistry Reviews*, vol. 301-302, pp. 123-133, 2015.
- [72] N. D. Chasteen *et al.*, "Vanadyl(IV) EPR Spin Probes Inorganic and Biochemical Aspects," *Biological Magnetic Resonance*, vol. 3, pp. 53-119, 1981.
- [73] Z. Strassberger *et al.*, "Synthesis, characterization and testing of a new V₂O₅/Al₂O₃–MgO catalyst for butane dehydrogenation and limonene oxidation," *Dalton Transactions*, vol. 42, pp. 5546-5553, 2013.
- [74] I. V. Kolbanev *et al.*, "Paramagnetic Centers Created Under Mechanochemical Treatment of Mixed Molybdenum-Vanadium Oxides," *Applied Magnetic Resonance*, vol. 47, pp. 575-588, 2016.

- [75] E. M. Modan *et al.*, "Advantages and disadvantages of chemical methods in the elaboration of nanomaterials," *The Annals of "Dunarea de Jos" University of Galati. Fascicle IX, Metallurgy and Materials Science*, vol. 43, pp. 53-60, 2020.
- [76] E. Novitskaya *et al.*, "A review of solution combustion synthesis: an analysis of parameters controlling powder characteristics," *International Materials Reviews*, vol. 66, pp. 188-214, 2021.
- [77] M. P. G. Mantilaka *et al.*, "Photocatalytic activity of electrospun MgO nanofibres: Synthesis, characterization and applications," *Materials Research Bulletin*, vol. 99, pp. 204-210, 2018.
- [78] W. L. Bragg, "The diffraction of short electromagnetic Waves by a Crystal," *Scientia*, vol. 23, p. 153, 1929.
- [79] D. A. Long, "Raman spectroscopy," *New York*, vol. 1, 1977.
- [80] S. J. Khambátá, "Raman Spectrum of Magnesium Oxide," *The Proceedings of the Physical Society*, vol. 69, Section A, 1956.
- [81] S. J. Pennycook *et al.*, *Scanning transmission electron microscopy: imaging and analysis*. Springer Science & Business Media, 2011.
- [82] S. Rana *et al.*, "Electron paramagnetic resonance spectroscopy in radiation research: Current status and perspectives," *Journal of Pharmacy And Bioallied Sciences*, vol. 2, p. 80, 2010.
- [83] T. Aoki, "Photoluminescence spectroscopy," *Characterization of Materials*, pp. 1-12, 2002.
- [84] A. J. Bard *et al.*, *Electrochemical methods: fundamentals and applications*: John Wiley & Sons, 2022.
- [85] R. M. Hazen, "Effects of temperature and pressure on the cell dimension and X-ray temperature factors of periclase," *American Mineralogist*, vol. 61, pp. 266-271, 1976.
- [86] S. Aksay, "Effects of Al dopant on XRD, FT-IR and UV-vis properties of MgO films," *Physica B: Condensed Matter*, vol. 570, pp. 280-284, 2019.
- [87] R. Dai *et al.*, "Antibacterial activity of V-doped rod-like MgO crystals decorated with nanoflake layer," *Ceramics International*, vol. 48, pp. 10579-10591, 2022.
- [88] S. Trukhanov *et al.*, "Cation ordering and magnetic properties of neodymium-barium manganites," *Technical Physics*, vol. 53, pp. 49-54, 2008.
- [89] A. Kozlovskiy *et al.*, "Optical and structural properties of AlN ceramics irradiated with heavy ions," *Optical Materials*, vol. 91, pp. 130-137, 2019.
- [90] Y. T. Prabhu *et al.*, "X-ray analysis by Williamson-Hall and size-strain plot methods of ZnO nanoparticles with fuel variation," *World Journal of Nano Science and Engineering*, vol. 2014, 2014.
- [91] C. Coulson, "Pauling's Chemical Bond," ed: Springer, 1961.
- [92] M. Simiari *et al.*, "Preparation and characterization of vanadium-doped nickel oxide nanostructure deposited by dip-coating technique," *The European Physical Journal Plus*, vol. 136, p. 517, 2021.

- [93] H. Letifi *et al.*, "Enhanced photocatalytic activity of vanadium-doped SnO₂ nanoparticles in rhodamine B degradation," *Advances in Condensed Matter Physics*, vol. 2019, pp. 1-11, 2019.
- [94] M. Nourmohammadian *et al.*, "Wettability behavior, photoluminescence and optical properties studies of nanostructured vanadium-doped magnesium oxide thin films: an effect of V concentrations," *Optical and Quantum Electronics*, vol. 55, p. 20, 2023.
- [95] S. Trukhanov *et al.*, "Magnetic properties of anion-deficient La_{1-x}Ba_xMnO₃ manganites," *Journal of Experimental and Theoretical Physics*, vol. 96, pp. 110-117, 2003.
- [96] A. Kozlovskiy *et al.*, "Evaluation of the efficiency of detection and capture of manganese in aqueous solutions of FeCeO_x nanocomposites doped with Nb₂O₅," *Sensors*, vol. 20, p. 4851, 2020.
- [97] K. Ishikawa *et al.*, "First-order Raman scattering in MgO microcrystals," *Journal of applied physics*, vol. 57, pp. 973-975, 1985.
- [98] T. Athar *et al.*, "Synthesis of MgO nanopowder via non aqueous sol-gel method," *Advanced Science Letters*, vol. 7, pp. 27-29, 2012.
- [99] P. Shvets *et al.*, "A review of Raman spectroscopy of vanadium oxides," *Journal of Raman spectroscopy*, vol. 50, pp. 1226-1244, 2019.
- [100] S. Visweswaran *et al.*, "Characterization of MgO thin film prepared by spray pyrolysis technique using perfume atomizer," *Journal of Materials Science: Materials in Electronics*, vol. 31, pp. 14838-14850, 2020.
- [101] D. Varshney *et al.*, "On the synthesis, structural, optical and magnetic properties of nano-size Zn-MgO," *Superlattices and Microstructures*, vol. 85, pp. 886-893, 2015.
- [102] V.-I. Merupo *et al.*, "Structural and optical characterization of ball-milled copper-doped bismuth vanadium oxide (BiVO₄)," *CrystEngComm*, vol. 17, pp. 3366-3375, 2015.
- [103] P. Shvets *et al.*, "Correlation between Raman spectra and oxygen content in amorphous vanadium oxides," *Physica B: Condensed Matter*, vol. 613, p. 412995, 2021.
- [104] D. M. Murphy *et al.*, "Surface defect sites formed on partially and fully dehydrated MgO: an EPR/ENDOR study," *The Journal of Physical Chemistry B*, vol. 103, pp. 1944-1953, 1999.
- [105] C. J. Magon *et al.*, "Deconvolution of the EPR spectra of vanadium oxide nanotubes," *Journal of Magnetic Resonance*, vol. 222, pp. 26-33, 2012.
- [106] A. Brückner, "In situ electron paramagnetic resonance: a unique tool for analyzing structure-reactivity relationships in heterogeneous catalysis," *Chemical Society Reviews*, vol. 39, pp. 4673-4684, 2010.
- [107] S. Heo *et al.*, "Band gap and defect states of MgO thin films investigated using reflection electron energy loss spectroscopy," *AIP Advances*, vol. 5, p. 077167, 2015.
- [108] K. Nemade *et al.*, "Synthesis of MgO nanoparticles by solvent mixed spray pyrolysis technique for optical investigation," *International Journal of Metals*, vol. 2014, pp. 1-4, 2014.

- [109] B. Nourozi *et al.*, "The electronic and optical properties of MgO mono-layer: Based on GGA-mBJ," *Results in Physics*, vol. 12, pp. 2038-2043, 2019.
- [110] O. Diachenko *et al.*, "Surface Morphology, Structural and Optical Properties of MgO Films Obtained by Spray Pyrolysis Technique," *Acta Physica Polonica A*, vol. 130, pp. 805-810, 2016.
- [111] M. Sarno, "Nanotechnology in energy storage: The supercapacitors," in *Studies in Surface Science and Catalysis*, vol. 179, pp. 431-458, 2020.
- [112] Z. S. Wu *et al.*, "Graphene-based in-plane micro-supercapacitors with high power and energy densities," *Nature communications*, vol. 4, p. 2487, 2013.
- [113] B. Saravanakumar *et al.*, "Surfactant effect on synthesis and electrochemical properties of nickel-doped magnesium oxide (Ni-MgO) for supercapacitor applications," *Applied Physics A*, vol. 123, pp. 1-9, 2017.
- [114] S. Petnikota *et al.*, "Electrochemistry-related aspects of safety of graphene-based non-aqueous electrochemical supercapacitors: A case study with MgO-decorated few-layer graphene as an electrode material," *New Journal of Chemistry*, vol. 43, pp. 9793-9801, 2019.
- [115] K. Karthikeyan *et al.*, "Microwave assisted green synthesis of MgO-carbon nanotube composites as electrode material for high power and energy density supercapacitors," *Journal of Materials Chemistry A*, vol. 1, pp. 4105-4111, 2013.
- [116] P. Kossyrev, "Carbon black supercapacitors employing thin electrodes," *Journal of Power Sources*, vol. 201, pp. 347-352, 2012.
- [117] Z. U. Rehman *et al.*, "Metal oxide-carbon composites for supercapacitor applications," in *Metal Oxide-Carbon Hybrid Materials*: Elsevier, pp. 133-177, 2022.
- [118] M. R. Pallavolu *et al.*, "Self-assembled and highly faceted growth of Mo and V doped ZnO nanoflowers for high-performance supercapacitors," *Journal of Alloys and Compounds*, vol. 886, p. 161234, 2021.
- [119] A. Hroub *et al.*, "Vanadium-doped magnesium oxide nanoparticles as electrodes in supercapacitor devices," *Journal of Alloys and Compounds*, vol. 958, p. 170442, 2023.